An Early Pennsylvanian thermal anomaly in the forearc of SW Gondwana: the origin of the Caleta Loa Metamorphic Complex, northern Chile (21°30’ S)

*Fernando Sepúlveda[1]; Paulina Vásquez[1]; Andrea Hemmelmann[2]; Gerhard Franz[2]

[1]*Servicio Nacional de Geología y Minería, Chile. Avenida Santa María 0104, Providencia, Santiago. fernando.sepulveda@sernageomin.cl, paulina.vasquez@sernageomin.cl*

[2]*Institut für Angewandte Geowissenschaften, Technische Universität Berlin, 10587 Berlin, Germany. andrea_bhh@hotmail.com, gerhard.franz@tu-berlin.de*

** Corresponding author: fernando.sepulveda@sernageomin.cl*

Abstract. This study presents a comprehensive characterization of the Lower Pennsylvanian Caleta Loa Metamorphic Complex (CLMC), located in the Coastal Cordillera of northern Chile at around 21°30’ S. Through integrated petrographic, geochemical, thermodynamic, and geochronological analyses, the research aims to constrain the pressure-temperature (P-T) conditions of migmatite formation, refine the protolith identity, and assess the regional geodynamic context of the complex. Thermodynamic modelling using P-T pseudosections and mineral composition reveals that the CLMC migmatites formed under upper amphibolite facies conditions, with peak estimates of approximately 3.3–3.4 kbar and 650 °C. These results are consistent with a high geothermal gradient and suggest a crustal depth of ~13 km during peak metamorphism. U-Pb detrital zircon age patterns indicate a

protolith sedimentation age no older than *ca.* 350 Ma (Early Mississippian), consistent with a genetic correlation with the nearby El Toco Formation, a low-grade metasedimentary unit in the forearc of the SW Gondwana margin. Structural data show evidence of compressional deformation, including top-to-the-west shear indicators and westward verging folds, which are interpreted as syn-anatectic features. These observations, combined with the metamorphic and geochronological data, point to a tectono-thermal event in the SW Gondwana forearc during the Early Pennsylvanian (*ca*. 318–316 Ma), associated with the so-called 'Toco Orogeny' and potentially linked to contemporaneous inland magmatic activity. The existence of this event supports a scenario of renewed subduction and/or the end of a magmatic lull along the proto-Pacific Gondwana margin. The current juxtaposition of the CLMC and the El Toco Formation on either side of a major fault suggests significant uplift and exhumation of the former prior to the Late Triassic.

Keywords: migmatites, P-T pseudosections, 'Toco Orogeny', Carboniferous, SW Gondwana.

Una anomalía termal del Pennsylvaniano Temprano en el antearco de Gondwana suroccidental: el origen del Complejo Metamórfico Caleta Loa, norte de Chile (21°30' S). Este estudio presenta una caracterización exhaustiva del Complejo Metamórfico Caleta Loa (CMCL), del Pennsilvaniano Inferior, situado en la Cordillera de la Costa del norte de Chile (~21°30' S). Mediante análisis integrados de petrografía, geoquímica, termodinámica y geocronología, la investigación tiene como objetivo determinar las condiciones de presión-temperatura (P-T) de la formación de sus migmatitas, refinar la identidad del protolito y

evaluar el contexto geodinámico regional del complejo. La modelización termodinámica, utilizando pseudosecciones P-T y composición mineral, revela que las migmatitas del CMCL se formaron en condiciones de facies anfibolita superior, con estimaciones máximas de aproximadamente 3,3–3,4 kbar y 650 °C. Estos resultados son consistentes con un gradiente geotérmico elevado y sugieren una profundidad cortical de aprox. 13 km durante el peak metamórfico. Los patrones de edad U-Pb de circones detríticos indican una edad máxima de sedimentación del protolito de *ca*. 350 Ma (Mississippiano Temprano), lo que concuerda con una correlación genética con la contigua Formación El Toco, unidad metasedimentaria de bajo grado metamórfico en el antearco del margen suroccidental de Gondwana. Los datos estructurales muestran evidencia de deformación compresiva, incluyendo indicadores de cizalle de bloque superior hacia el oeste y pliegues con vergencia hacia el oeste, que se interpretan como características sinanatécticas. Estas observaciones, combinadas con datos metamórficos y geocronológicos, apuntan a un evento tectono-termal en el antearco de Gondwana suroccidental durante el Pennsylvaniano temprano (*ca*. 318–316 Ma), asociado a la denominada "Orogenia Toco" y potencialmente vinculado a actividad magmática continental contemporánea. La existencia de este evento respalda un escenario de subducción renovada y/o el fin de una fase de calma magmática a lo largo del margen proto-Pacífico de Gondwana. La yuxtaposición actual del CMCL y de la Formación El Toco a ambos lados de una falla importante sugiere alzamiento y exhumación significativos del CMCL antes del Triásico Tardío.

Palabras clave: migmatitas, pseudosecciones P-T, "Orogenia Toco", Carbonífero, Gondwana suroccidental.

Introduction

The western margin of South America once formed the SW margin of Gondwana (Fig. 1A). This area has been regarded as an active margin for almost the entire Palaeozoic Era, associated with the collision of tectono-stratigraphic terranes that were amalgamated to the supercontinent (*e.g.*, Dalziel and Forsythe, 1985; Mpodozis and Ramos, 1989; Bahlburg and Hervé, 1997; Ramos, 2009). These successive events were part of the intercontinental accretionary Terra Australis Orogeny (Cawood, 2005), associated with changes in the conditions of subduction of the proto-Pacific oceanic plate under the continental margin of Gondwana (Vaughan *et al.*, 2005). Although some of these events are well studied and constrained in time, others are yet to be completely understood. The 'Toco Orogeny' (Bahlburg and Breitkreuz, 1991), for instance, is one of the latter, recorded in Upper Devonian-Lower Carboniferous low-grade marine metasedimentary successions of the Coastal Cordillera of northern Chile.

In northern Chile (18–32° S), several Palaeozoic metamorphic complexes are found as part of the SW Gondwana margin, in both the Coastal Cordillera and the Main Cordillera (e.g., Hervé *et al.*, 2007; Pankhurst *et al.*, 2016; Díaz-Alvarado *et al*., 2019; Creixell *et al.*, 2021) (Fig. 1B). The Caleta Loa Metamorphic Complex (CLMC, Vásquez *et al.*, 2018; Fig. 1C), in the Coastal Cordillera, is a migmatite complex that provides evidence of a Late Carboniferous high-temperature magmatic/tectonic event. It is the northernmost example of melt generation associated with subduction at the SW Gondwana margin after the Devonian Period (see Creixell *et al.* 2021).

The Devonian Period has traditionally been regarded as a passive margin stage in the south-central Andean region of the Gondwana margin (*e.g.*, Bahlburg and Hervé, 1997; Cawood, 2005; Bahlburg *et al.*, 2009). This is supported by the absence or scarcity of Devonian detrital zircon grains along the proto-Andean margin from northern Peru to central Chile (*e.g.*, Hervé *et al.*, 2013; Bahlburg *et al.*, 2009; Reimann *et al.*, 2010; Augustsson *et al.*, 2015; Einhorn *et al.*, 2015), and by the lack of evidence of coeval magmatism, deformation or metamorphism (Bahlburg and Hervé, 1997; Lucassen *et al.*, 2000; Chew *et al.*, 2007; Cardona *et al.*, 2009). Nevertheless, some authors suggested that the absence (or scarcity) of Devonian detrital zircons is a consequence of an inland (eastward) migration of the magmatic arc front during this period (*e.g.*, Charrier *et al.*, 2007; Dahlquist *et al.*, 2018). These proposals, however, do not consider the tectonic and magmatic segmentation of the Gondwana margin (*e.g.*, Calderón *et al.*, 2020; Dahlquist *et al*., 2021; Creixell *et al*., 2025). Recently, Bahlburg (2022) proposed that there was an active margin here during the Devonian, and that the scarcity of Silurian- and Devonian-aged zircons is due to a decrease in magmatic activity (magmatic lull phase) during these periods.

The relation between the CLMC and the low-grade metasedimentary units of the late Palaeozoic Gondwana margin is unclear, as are the P-T metamorphic conditions of formation of the CLMC and the geodynamic implications of this process. There are also no accurate data on the timing of the deformation/metamorphism directly related to the 'Toco Orogeny'.

The aim of this paper is to determine and quantify the P-T conditions of formation of the migmatites of the CLMC, using thermodynamic calculations of mineral equilibrium (P-T

pseudosections; Perple_X; Connolly, 2005) and geothermometers based on the mineral chemistry. New U-Pb detrital zircon ages and structural data were obtained in order to identify the protolith and the regional geological context of these rocks. Collectively, these findings help constrain the timing and nature of the 'Toco Orogeny', demonstrating its link with the development of the CLMC, and provide insights into the geodynamic evolution of the middle to late Palaeozoic proto-Pacific margin of Gondwana in this area.

Geological overview

Outcrops of Palaeozoic rocks in the Coastal Cordillera of northernmost Chile (18°30' – 24°00' S) are very limited in comparison with those of Mesozoic rocks (Sernageomin, 2002). The former comprise a variety of low-grade deformed Upper Devonian to lowest Carboniferous metasedimentary units, Upper Carboniferous granitic plutonic rocks, and scarce migmatites of the same age. The metasedimentary units are the El Toco (Harrington, 1961) and the Sierra del Tigre (Niemeyer *et al.*, 1997) formations, which represent turbiditic marine deposits of the SW Gondwana margin (Bahlburg and Breitkreuz, 1993; Bahlburg and Hervé, 1997; Niemeyer *et al.*, 1997).

The restricted migmatite outcrops have been known since the early 1990s (*cf*. Lucassen *et al.*, 1994) and were lately defined as the CLMC by Vásquez *et al.* (2018). The rocks of the CLMC in the Río Loa canyon, near its mouth, were first described by Lucassen *et al.* (1994, 1996) and Wilke *et al.* (1997). They identified stromatic migmatites with sparse intercalations of equigranular gneisses, pegmatitic layers, and dioritic orthogneisses

(amphibolites). Lucassen *et al.* (1996) determined peak metamorphic temperature conditions of 600–750 °C, and low-pressure conditions were suggested (Lucassen *et al.*, 1996, 2000; Wilke *et al.*, 1997).

Vásquez *et al.* (2018) showed that this complex extends continuously along the Río Loa canyon from near its mouth eastwards to the main trace of the Atacama Fault System (AFS; see Skarmeta and Marinovic, 1981), as well as in the hills adjacent to the canyon in the western part of the Coastal Cordillera (Figs. 1C and 2A). The base of the CLMC is not exposed. Its outcrops are covered by Upper Triassic-Lower Jurassic volcanic rocks and it is intruded by Upper Jurassic and Lower Cretaceous plutonic bodies. The AFS separates the CLMC from the El Toco Formation to the east (Fig. 1C). Vásquez *et al.* (2018) described the CLMC as mainly composed of stromatic metatexitic migmatites and diatexitic migmatites. However, the lithology of the CLMC is re-evaluated in this study, redefining it as composed of stromatic metatexitic migmatites and rare gneisses only, with predominant and continuous layer-parallel bands of leucosome at outcrop scale (see Fig. 2). Three samples of the CLMC previously yielded zircon U-Pb ages of *ca*. 318–316 Ma (Pankhurst *et al.*, 2016; Vásquez *et al.*, 2018), which were taken as the age of metamorphism and migmatite formation. Younger K-Ar biotite ages (*ca.* 189 and 170 Ma; Lucassen *et al.*, 2000) are interpreted as reset by Jurassic magmatic activity. The U-Pb zircon age patterns obtained by Pankhurst *et al*. (2016) are similar to those of local detrital samples (*e.g*., Sierra del Tigre Formation); together with the metamorphic mineral assemblages (see below), they indicate a sedimentary protolith for the migmatites of the CLMC.

Methodology

Six rock samples from the melanosome of the CLMC were studied petrographically as summarised in Table 1. They were classified as biotite-gneiss (GSS-208, GSS-267), biotite-sillimanite gneiss (GSS-31), biotite-garnet gneiss (3/278, 3/347), and dioritic orthogneiss (3/276). Two of these (GSS-31 and GSS-208) were analysed for whole-rock geochemistry (Table 2), and five for mineral chemistry: two by scanning electron microscopy (SEM) with energy-dispersive spectroscopy (EDS) (GSS-31 and GSS-208; Supplementary Table 1) and five by electron probe microanalyzer (EPMA) (GSS-31, GSS-208, 3/276, 3/278, and 3/347; Supplementary Table 2). Analytical techniques are described in Appendix A.

Pseudosection modelling

In order to determine the P-T conditions of the CLMC, P-T pseudosections were constructed with the Perple_X software package (Connolly, 2005; version from September 2018 downloaded from http://www.perplex.ethz.ch/) using the bulk rock composition of samples GSS-31 and GSS-208 (Table 2). The metamorphic mineral assemblage of these samples is sillimanite+biotite+plagioclase+K-feldspar+quartz+cordierite+ilmenite (Table 1). Calculations were carried out in the Mn-Na-Ti-Ca-K-Fe-Mg-Al-Si-H-O system using the thermodynamic database of Holland and Powell (1998, updated in 2002) for minerals and H_2O (model CORK: Holland and Powell, 1991). A P-T range of 1–6 kbar and 500–800 °C was considered for the P-T pseudosections. After the construction of the pseudosections, they were contoured with isopleths for various modal (melt content) and chemical (*e.g.*, Si content of white mica) parameters by applying the sub-programs *werami* and *pstable*. The

171 final pseudosections and contoured P-T diagrams were redrawn by smoothing curves as
172 demonstrated by Connolly (2005).

173 The following solid solution models (see Powell and Holland, 1999) compatible with this
174 data set were selected: Gt(HP) for garnet, Bio(WPH) for biotite, IlGkPy for ilmenite,
175 Pheng(HP) for white mica, Mica(M) for paragonite, hCrd for cordierite, feldspar for
176 feldspars, Opx(HP) for orthopyroxene, Cpx(HP) for clinopyroxene, St(HP) for staurolite,
177 Chl(HP) for chlorite, Ep(HP) for epidote, and GlTrTsPg for amphibole. For the silicate melt,
178 the haplogranitic melt model melt (HP) was applied (White *et al.* 2001). The fluid was
179 considered to be pure H_2O.

180 The composition of the studied samples was modified to fit the 11-component system: P_2O_5
181 was fractionated as apatite, together with the corresponding amount of CaO. All Fe was
182 considered as divalent, owing to the lack of Fe^{3+}-rich oxides and the negligible amount of
183 Fe^{3+} in the analysed minerals. Oxygen content (O_2) was set to 0.02 for sample GSS-31 and
184 neglected (O_2=0) for sample GSS-208, due to the absence of magnetite, the low amount of
185 ferric iron in minerals, and the presence of ilmenite in the metamorphic association, which
186 indicate low oxidation conditions (*e.g.*, Diener and Powell, 2010). Different values of H_2O
187 (between 1 and 4 wt.%) and O_2 (0–0.05 wt.%, maximum value corresponding to 10% Fe^{3+} of
188 the total iron; see Massonne *et al.*, 2007) were considered during preliminary calculations.
189 The variation of O_2 content resulted in minor changes of the pseudosections topology, with
190 no significant changes in the considered phase-in boundaries. Most notable changes in
191 these boundaries were related to variations in the amount of H_2O, such as the appearance
192 of garnet below 500 °C at high pressures or above 650 °C at low pressures, or the existence

193 of white mica at relatively high temperatures. For the final calculations, the water content
194 was set to a maximum of 3 wt.% to guarantee a free hydrous fluid phase. The melt volume
195 was used to constrain the P-T conditions, with a maximum of 20 vol.%, which is near the
196 upper limit defined for stromatic migmatites (White *et al.*, 2005; Sawyer, 2008), and agrees
197 with our field observations.

198 Since uncertainties of 10% on the P- and 5% on the T-estimates resulting from
199 pseudosection modelling have been reported (*e.g.*, Massonne, 2013), our T data were
200 compared with the temperature range obtained through Ti in biotite geothermometers.

201 Zircon U-Pb LA-ICP-MS geochronology

202 U-Pb isotopic composition of zircons from melanosome sample GSS-267 was obtained by
203 LA-ICP-MS (laser ablation-inductively coupled-mass spectrometry) at the Isotopic Geology
204 Laboratory of Sernageomin. The sample was crushed and pulverized in a Retsch pulverizer
205 to ≤500 µm. Heavy mineral concentration was made using a Gemini table followed by hand-
206 picking under UV lamp (Suárez *et al*., 2015). A random selection of 100 hand-picked zircon
207 grains was mounted for polishing on a 2.5 cm diameter epoxy resin disc together with
208 Temora-2 standard zircon (Black *et al.*, 2004). Cathodoluminescence (CL) SEM images were
209 obtained using a Zeiss MA-10 Scanning Electronic Microscope, with a Gatan ChromaCL2 UV
210 CL detector and a Zeiss annular BSE (backscattered electron) detector. Zircon grains were
211 ablated using a Photon Machines Analyte G2 193 nm ArF (Argon Fluoride) excimer ablation
212 system coupled to a Thermo Scientific Element XR ICP-MS system with the following
213 parameters: 30 µm beam size, 10 Hz repetition rate, and a beam energy density of 6 J/cm^2.

The depth of each ablation pit was 15-20 microns. U, Pb, and Th concentrations were calculated relative to the reference zircon GJ-1 (Jackson *et al.* 2004). Following baseline correction, the Pb/U ratios were corrected for downhole fractionation and normalized to reference zircon GJ-1. The data were reduced following procedures given in Williams (1998) using the Iolite software (Petrus and Kamber, 2012). Probability density and Concordia plots were carried out using the Isoplot macro (Ludwig, 2012). $^{206}Pb/^{238}U$ ages were corrected for common Pb by using measured ^{207}Pb (Williams, 1998). Radial plots and Maximum Likelihood Age (MLA; Vermeesch, 2021) were calculated with IsoplotR (Vermeesch, 2018). Reported uncertainties were always given at the 2σ level.

Results

Lithological and structural features

The leucosome is present as layer-parallel bands, dykes, sills, and veins, and metric-scale blobs (Fig. 2B-E). The layer-parallel bands are fine- to coarse-grained, and their thickness is irregular, varying between 0.2 to 10.0 cm, defining a compositional banding foliation (Fig. 2C, F). At outcrop scale, the contacts between these leucosome bands and the melanosome are diffused to stepped, locally sharp (*sensu* Pawley *et al.*, 2015). Leucosome dykes, sills and veins are discontinuously distributed within the metamorphic complex, varying in thickness from a few centimetres up to decimetres. In general, they have sharp stepped margins, with scarce cases of a sharp straight-edged margin. In some cases, dykes and sills have a millimetric biotite-rich narrow selvedge, suggesting late melting. Locally, in the upper

sections of the Río Loa canyon, the dykes fed metric scale leucosome bodies. The dykes cut the melanosome at moderate to high angles (~45°–90°; Fig. 2D, E). The modal composition of the coarse-grained leucosome corresponds to granite with variable proportions of biotite (1–5%) and muscovite (1–3%), whereas rare metric leucosome bodies correspond to biotite-muscovite-garnet granite (5% garnet). As no occurrences of leucosome have been observed outside the metamorphic complex, it has been classified as *in situ* and in-source leucosome (*sensu* Sawyer, 2008). The melanosome occurs as highly deformed, dark biotite-rich domains with sub-millimetric to millimetric granoblastic domains. The lepidoblastic domain includes sillimanite, ilmenite and scarce cordierite, as well as white mica replacing former biotite and sillimanite.

The foliation (S_1) in the CLMC is orientated mainly N-S, with 20° to 86° E dips. E-W and NNE-SSW strike variations are also observed, with 5° to 60° N to NW dips. Locally, the foliation is affected by discrete low-angle, occasionally melt-filled, reverse shear bands (Fig. 2C, F, G; Appendix B). These bands generated upright, moderately inclined to recumbent folds, of centimetric to decametric scale, whose axial planes generally trend N-S and dip 5° to 50° E, indicating westward vergence. Late leucosome sills, with mafic selvedge, are also affected by this folding. Occasionally, these folds exhibit an S_2 foliation that is parallel or at a low angle (<30°) to the S_1 (locally transposed) foliation (Fig. 2G; Appendix B). Blobs of leucosome were observed at the hinge of folds and other similar dilatational sites. Syn-tectonic feldspar porphyroblasts with pressure shadows also indicate a top-to-the west sense of shear (Fig. 2F, H; Appendix B).

Petrographical characteristics

Thirty thin sections with leucosome and melanosome in the same proportion were examined. In the melanosome, the foliation is parallel spaced and locally anastomosed, defined by grano-lepidoblastic levels formed by biotite (85–90%), white mica (0–10%), and rare sillimanite bundles (fibrolite; <5%) (Fig. 3A, B). Biotite and white mica crystals display kink-bands. Irregular-shaped to elongated grains of quartz, with less plagioclase, K-feldspar, and scarce altered cordierite (<2%) are also present. Biotite and white mica occur with a preferred orientation within leucocratic granoblastic pods in the melanosome among anhedral quartz, plagioclase and K-feldspar crystals. Aggregates of biotite, white mica and ilmenite intergrowths are observed as well. Quartz and/or plagioclase porphyroblasts develop sigma-type structures of fine-grained quartz and white mica, indicating a sinistral (top-to-the west) sense of shear.

Leucosome layers parallel to the main foliation are made up of quartz (50–80%), plagioclase (10–30%) and K-feldspar (locally microcline) (10–15%), with minor (≤5%) biotite and white mica. The granoblastic crystals exhibit serrated to lobate grain boundaries and quartz shows undulose extinction (locally chessboard extinction), suggesting deformation, dynamic recovery, and grain boundary migration during recrystallisation. Biotite and white mica crystals also display kink-bands. Plagioclase locally shows secondary white mica growing along its cleavages, whereas K-feldspar is highly altered to sericite, and biotite to chlorite, with sericite-filled fractures cutting the foliation.

Two samples (3/278 and 3/347) show garnet and biotite porphyroblasts in a matrix of plagioclase, quartz, biotite and white mica, suggesting distinctive paleosome composition. The garnet crystals have predominant almandine composition (see Supplementary Table 2),

279 are ~2.0–2.5 mm in size and partly idiomorphic, exhibiting numerous inclusions of biotite
280 and retrograde chlorite at the edges and along cracks.

281 In cleavages and/or at chlorite alteration zones, biotite crystals exhibit sagenitic rutile
282 crystals. Ilmenite is the stable Ti-rich phase, generally occurring disseminated with a
283 preferred orientation. Accessory phases are apatite, monazite, zircon and graphite.

284 Several microstructures indicate that samples underwent melting processes (see Holness *et*
285 *al.*, 2011): 1) undulose (locally chessboard) extinction of quartz and irregular to lobate grain
286 boundaries of quartz and plagioclase (Fig. 3A, C); 2) films and "branching" grains of K-
287 feldspar between quartz crystals (Fig. 3D); 3) isolated faceted grain boundaries of
288 plagioclase; 4) cuspate low dihedral angles in quartz crystals (Fig. 3D) ; 5) "string of beads"
289 of quartz (Fig. 3E); and 6) corroded quartz and plagioclase grains (Fig. 3F)

290 The inferred peak metamorphic mineral assemblage is considered to have been
291 sillimanite+biotite+plagioclase+K-feldspar+quartz+cordierite+ilmenite (+melt), whereas for
292 garnet-bearing samples the peak metamorphic assemblage is
293 garnet+biotite+plagioclase+quartz+ilmenite (+melt) (Table 1). White mica (muscovite, see
294 below) is considered a post-peak phase developed during subsequent decompression
295 and/or cooling. White mica in fractures and in cleavages and chlorite suggests very late fluid
296 infiltration.

297 Mineral chemistry

298 Five migmatite samples were chosen for mineral chemistry (GSS-31, GSS-208, 3/276, 3/278
299 and 3/347; Hemmelmann, 2018). Representative EPMA analyses of two samples (GSS-31

and GSS-208) for which pseudosections were elaborated are presented in Table 2. The rest of the analyses are available in Supplementary Table 2.

Muscovite was analysed in samples GSS-31, GSS-208 and 3/276. The content of Si varies between 3.00 and 3.11 per formula unit (pfu), X_{Mg} = 0.43–0.56, and Ti contents as high as 0.07 pfu.

Garnet in samples 3/278 and 3/347 is mainly almandine (74–80 vol.%), with 10–18 vol.% pyrope, 4–7 vol.% grossular and 3–5 vol.% spessartine. X_{Mg} is less than 0.2, with higher values in cores. In sample 3/278, the proportion of almandine is 76–80%, whereas in sample 3/347 is 74–77%. The absence of zonation in the core of the crystals suggests chemical diffusion processes, whereas the strong decrease in MgO at the rim is indicative of retrograde metamorphism (see Fig. 3G).

Biotite crystals show similar compositions in all analysed samples, though biotite inclusions in garnet (samples 3/278 and 3/347) have lower Mg and higher Ti contents, and biotite from sample GSS-31 is richer in Mg. On the basis of 22 oxygen atoms in the structural formula, the biotite composition is defined by: Si = 5.286–5.730 pfu, X_{Mg} = 0.36–0.46, and Ti = 0.0–0.53 pfu. Sample 3/347 is strongly chloritized.

The composition of plagioclase varies notably among samples: plagioclase from sample GSS-31 is oligoclase (An17-An27), in sample 3/347 the composition is An48-An51, and sample 3/276 contains labradorite (An49-An60) and bytownite (An81-An86), with centres of almost pure anorthite.

Amphibole is present only in sample 3/276 and is grunerite (after Hawthorne *et al.*, 2012), with Si = 7.76–7.84 pfu, Al_{IV} = 0.16–0.24, Fe=3.44–3.55 pfu, X_{Mg} = 0.47–0.48, Ti = 0.01, and Na = 0.03–0.06 pfu.

Ilmenite was analysed in sample GSS-208, showing a Mn content of 0.21 pfu. In general, it is present as fine elongated crystals within the cleavage of biotite. Sillimanite and monazite (samples GSS-31 and GSS-208), cordierite (sample GSS-208) and F-apatite (samples GSS-208 and 3/278) were observed as well.

Geothermometry

Ti-in-biotite geothermometry was performed on samples 3/347, 3/276, GSS-208, and GSS-31 (Table 1), applying the calibrations of Henry *et al.* (2005) and Wu and Chen (2015). The pressure for the Wu and Chen (2015) geothermometer was set to 0.4 GPa based on the preliminary results from pseudosections (see below). This geothermometer is optimised for ilmenite- and/or rutile-bearing samples, making it suitable for the selected samples. All Fe was considered to be divalent, based on the lack of Fe^{3+} bearing phases. Temperatures obtained for sample 3/347 are 663–728 °C (mean=686 °C) using the geothermometer of Henry *et al.* (2005), and 606–702 °C (mean=654 °C) using the method of Wu and Chen (2015). For sample 3/276, the equivalent results are 655 °C and 577 °C, respectively, for sample GSS-208 they are 581 °C and 583 °C, and for sample GSS-31 they fluctuate between 600 and 666 °C (mean=638 °C) and 566 and 642 °C (mean=608 °C). It is noteworthy that the application of the geothermometer of Henry *et al.* (2005) yielded systematically higher temperatures (up to 78 °C) than those using Wu and Chen (2015) (see Supplementary Table

2). Sagenitic rutile and/or chlorite within biotite crystals were observed in several thin sections, indicating retrograde mineral reactions. According to Henry *et al.* (2005), in these cases, the application of Ti-in-biotite geothermometers could result in anomalously low temperature estimates compared to other geothermometers. Nevertheless, the temperatures obtained here using this method are only slightly lower than those calculated using pseudosections (see below).

Pseudosection modelling and P-T constraints

The P-T pseudosections for GSS-31 and GSS-208 are shown in figures 4 and 5. P-T conditions were derived by projecting the XFe = Fe/(Fe+Mg) isopleth of biotite onto the P-T field of the peak metamorphic mineral assemblage and intersecting it with the melt content within the same P-T field. The Si isopleths of muscovite were also calculated, but the analysed Si content lied outside the P-T field of the peak metamorphic mineral assemblage, showing that it is a retrograde phase (see below).

For sample GSS-31 (Fig. 4), the XFe isopleth of biotite with the observed XFe content (mean=0.57 pfu) projects very close to the limit of the P-T field of the peak metamorphic mineral assemblage in this sample (biotite+sillimanite+quartz+albite+K-feldspar+ilmenite), within a contiguous field containing additional cordierite. The amount of cordierite in this P-T field is <5%., so it is probable that this mineral is present in the sample in very low amounts, which is supported by its presence in sample GSS-208 (Table 1). The intersection of the observed XFe content in biotite with this P-T field gives a range of about 3.35–3.40 kbar and 650–655 °C. The isopleths of ~10% melt also plot in the same P-T field. Moreover,

362 the calculated plagioclase composition in the P-T field of the observed assemblage matches
363 the observed composition (Ab72-Ab73). On the other side, the Si isopleth of muscovite from
364 sample GSS-31 with the observed Si content (mean=3.02 pfu) lies below 1.8 kbar at ~480–
365 550 °C, *i.e.*, lower P-T conditions than those determined for the P-T field of the observed
366 mineral assemblage, which indicates that the analysed crystals grew under retrograde
367 metamorphism or hydrothermal alteration, as noticed in the petrographic analysis. Due to
368 the election of O_2>0 in the calculations for this sample, magnetite is ubiquitous across all
369 the P-T ranges, but always below 0.16%.

370 For sample GSS-208 (Fig. 5), the XFe isopleth of biotite matches the analysed XFe (~0.6 pfu)
371 inside the P-T field of the observed mineral assemblage, at around 3.3–3.4 kbar and 640–
372 650 °C, implying equilibrium. The isopleths of melt (10–20%) intersect the XFe isopleths of
373 biotite on a narrow strip within the P-T field of the observed mineral assemblage, which
374 yields a restricted P-T range of 3.30–3.35 kbar and 645 °C. On the other hand, two chemical
375 analyses of muscovite did not provide proper stoichiometric results to estimate the P
376 conditions (see Table 2).

377 In both pseudosections, the garnet stability is limited to higher temperatures (>680 °C)
378 and/or higher pressures (P>4.5 kbar) (see figures 4 and 5).

379 Geochronology

380 A sample of the melanosome of the CLMC (sample GSS-267) was analysed by LA-ICP-MS U-
381 Pb on inherited detrital zircons (Fig. 6A-C). The sample was collected from an outcrop near
382 where sample GSS-31 was taken, and consists mainly of biotite, quartz, plagioclase, K-

feldspar, and muscovite, with ilmenite, zircon and apatite as accessories (Table 1). In general, zircon grains are elongated with rounded to subrounded edges, with a few with angular edges. They display complex internal zoning at the CL images (Fig. 6B). All 100 zircon grains analysed were included in the results (see Supplementary Table 3). Th/U ratios are between 0.08 and 5.27, generally indicative of igneous zircons from multiple sources. The apparent ages range from *ca*. 368 to 2625 Ma. The youngest peak in the age pattern is *ca.* 450 Ma; there is also a significant grouping at 470 Ma and two prominent older peaks at 1050 Ma and 1350 Ma (Fig. 6A). The Maximum Likelihood Age (MLA; Vermeesch, 2021) is *ca*. 369±10 Ma (Supplementary Table 3), interpreted here as the oldest possible sedimentation age of the protolith of these metamorphic rocks.

Discussion

P-T conditions

The peak of metamorphism of the CLMC was attained at ~3.3–3.4 kbar and ~650 °C, under upper amphibolite facies conditions, implying a low P/T gradient. The temperatures determined by pseudosections agree with those obtained using other geothermometers (Ti-in-biotite), as well as being within the range of 600–750 °C reported by Lucassen *et al.* (1996) using an unspecified garnet-biotite geothermometer. Our pressure determination is in line with the observations of Lucassen *et al.* (1996, 1999, 2000), who indicated regional low-P metamorphic conditions due to the absence or minor presence of garnet. Assuming an average upper crustal density of 2,700 kg/m^3 (*e.g.*, Lucassen *et al*., 2001), a depth of ~13

404 km and a high geothermal gradient of ~52 °C/km can be derived from calculated
405 metamorphic pressure conditions.

406 The presence of garnet in migmatite samples 3/278 and 3/347 suggests that this phase is
407 either a remnant from an earlier stage of migmatisation at slightly higher P, or
408 metamorphism of a paleosome with a composition different to that of the surrounding
409 rocks. If garnet did grow before the observed mineral assemblage reached equilibrium at
410 3.3–3.4 kbar and 650 °C, the calculated P range would be a minimum. The occurrence of
411 garnet in isolated leucosome outcrops indicates growth under peritectic conditions (*e.g.*,
412 Stevens *et al.*, 2007), which would support this interpretation. However, a local particular
413 paleosome richer in Fe than that of the samples used in the pseudosections cannot be ruled
414 out, which would be necessary to equilibrate almandine garnet at P similar to that obtained
415 by the pseudosections.

416 The pressure deduced from the Si content of muscovite (sample GSS-31) is below 1.8 kbar
417 and outside the peak P-T range. Considering that the CLMC was already exhumed by the
418 Late Triassic, this pressure could be attributed either to a retrograde reaction after the
419 metamorphic peak, or to low-grade alteration associated with granitic intrusions that crop
420 out in the Coastal Cordillera in the vicinity of the study area (Sepúlveda *et al.*, 2014; Vásquez
421 *et al.*, 2018) (Fig. 1C), and were part of the extensive Late Carboniferous-Early Permian
422 igneous activity (310–260 Ma, Maksaev *et al.*, 2014).

423 The P-T conditions determined here strongly contrast with those inferred for the late
424 Palaeozoic forearc metasedimentary units of the SW Gondwana margin in the Coastal

Cordillera of northern Chile (18–24° S). The latter are deformed, low-grade sedimentary rocks (*e.g.*, Bahlburg and Breitkreuz, 1991), with metamorphic paragenesis that includes chlorite, white mica, albite and quartz (*e.g.*, Bobenrieth, 1980; Skarmeta and Marinovic, 1981; Bahlburg, 1987; Niemeyer *et al.*, 1997).

Protolith of the CLMC

The two most prominent older peaks of the U-Pb detrital zircon age pattern of sample GSS-267 (1050 and 1350 Ma; Fig. 6A) are similar to the main Mesoproterozoic age components in the protolith of the Sierra de Moreno Metamorphic Complex (Aguilef *et al.*, 2019), a migmatite-bearing unit that forms the Precambrian to early Palaeozoic basement of the Precordillera at the same latitude. This unit has traditionally been considered as part of the basement of the Antofalla crustal block (*e.g.*, Loewy *et al.*, 2004; Ramos, 2008, 2010), where U-Pb detrital zircon age populations have been determined for the sedimentary protolith of the migmatites at *ca.* 1250 and 1200 Ma (Damm *et al.*, 1990), *ca.* 1025, 1140, 1170, and 1460 Ma (Pankhurst *et al.*, 2016), *ca.* 1000, 1060, and 1180 Ma (Aguilef *et al.*, 2019), and *ca.* 1050 and 1160 Ma (Sepúlveda *et al.*, 2024).

The Palaeozoic zircon ages show significant clusters at *ca.* 450 and 470 Ma (Fig. 6A, E). These ages were identified in the detrital zircon age pattern of the samples from the CLMC analysed by Pankhurst *et al.* (2016), as well as in the neighbouring El Toco and Sierra del Tigre formations (Bahlburg *et al.*, 2009; Augustsson *et al.*, 2015; Einhorn *et al.*, 2015, Pankhurst *et al.*, 2016; Antofagasta Minerals *in* Baeza and Astudillo, 2019). These ages are ubiquitous in all late Palaeozoic metasedimentary units in northern Chile (see Bahlburg *et*

446 *al.* 2009; Pankhurst *et al*., 2016; Creixell *et al.*, 2021) and represent the magmatic products
447 of the Famatinian continental arc (Pankhurst *et al*., 1998; Ramos, 2008; Rapela *et al.*, 2018).

448 When the Early Pennsylvanian ages representing migmatite formation (*ca.* 318–316 Ma;
449 Pankhurst *et al.*, 2016; Vásquez *et al.*, 2018) are filtered out, the Palaeozoic U-Pb detrital
450 zircon age patterns of the CLMC exhibit a prominent peak at *ca.* 350 Ma (Early
451 Mississippian), as well as a lesser peak at *ca*. 380 Ma (Late Devonian) (Fig. 6E). Therefore,
452 the maximum depositional age of the protolith of CLMC is restricted to the Early
453 Mississippian (*ca*. 350 Ma), which is even younger than the Maximum Likelihood Age (MLA,
454 *ca*. 370 Ma) calculated for the sample of the CLMC analysed in this study.

455 A cluster at *ca*. 350 Ma was also identified in the U-Pb detrital zircon data from a sample of
456 the El Toco Formation (Augustsson *et al*., 2015). The composite U-Pb detrital zircon age
457 pattern of this unit (Fig. 6F) shows a Late Devonian peak (*ca*. 380 Ma). The Early
458 Carboniferous maximum depositional age contrasts with the Upper Devonian
459 biostratigraphic age of this unit (based on the presence of plant fossils; Moisan *et al*., 2011).
460 Notably, both the geochronological and the fossil samples were collected from the same
461 locality (Cerro Puntillas: 21°58’ S; 69°47’ W).

462 Late Devonian (*ca*. 370 Ma) and Early to Middle Mississippian (*ca*. 350, 344, and 335 Ma)
463 maximum depositional ages have been determined in the Sierra del Tigre Formation
464 (Antofagasta Minerals *in* Baeza and Astudillo, 2019), which are coherent with the maximum
465 depositional age of *ca*. 380 Ma (MLA; Supplementary Table 4) calculated in this study for
466 the sample of this unit analysed by Augustsson *et al*. (2015). There are no reports of plant

467 fossils in the Sierra del Tigre Formation. Its age was initially assumed as Devonian sustained
468 on an incomplete brachiopod fossil, tentatively assigned to *Mucrospirifer*(?) sp. (V.
469 Covacevich *in* Ferraris and Di Biase, 1978), and later supported by lithostratigraphic
470 correlation with the El Toco Formation (Niemeyer *et al*., 1997). However, the
471 biostratigraphic range of the *Mucrospirifer* genus now extends into the Early Mississippian
472 (Chen, 2010; Chen and Qing, 2024).

473 Despite the current inconsistencies between maximum depositional ages and
474 biostratigraphic ages, the similarities between the Palaeozoic peaks in the U-Pb detrital
475 zircon patterns of the CLMC and the El Toco Formation (and its southern equivalent, the
476 Sierra del Tigre Formation) (Fig. 6A, D), together with the proximity of their outcrops
477 (separated only by the main trace of the AFS; see Fig. 1C), allow us to infer that the protolith
478 of the CLMC consisted of rocks of the El Toco Formation that were migmatised at upper
479 crustal depths (~13 km) during the Early Pennsylvanian.

480 The Early Mississippian (*ca.* 350 Ma) age population marks the onset of the late Palaeozoic
481 magmatic arc (*e.g*., Creixell *et al.*, 2021) or the Gondwanide magmatic flare-up (Bahlburg,
482 2022). In contrast, age clusters at *ca.* 370–380 Ma in the detrital zircon age distribution of
483 the CLMC indicate the existence of a yet unrevealed Late Devonian magmatic source, whose
484 products are also evident in the U-Pb detrital zircon data of the Devonian-Carboniferous
485 Zorritas and Sierra de Argomedo formations (Augustsson *et al*., 2015). In this context, a
486 Devonian-Carboniferous active margin setting has recently been argued for SW Gondwana
487 by Bahlburg (2022) and García Zavaleta *et al.* (2024). The latter authors inferred a shift from

488 flat-slab subduction during the Devonian to normal subduction in the Carboniferous.
489 Although scarce, Devonian detrital zircons have also been reported farther east, in the late
490 Palaeozoic Tarija Basin of southern Bolivia (22° S) by Calle *et al.* (2023) and Ferroni *et al.*
491 (2025), indicating the presence of a magmatic source that fed this foreland basin from the
492 west. Dahlquist *et al.* (2021, and references therein) also proposed the existence of a
493 Devonian calc-alkaline magmatic arc in the Frontal Cordillera of Argentina, albeit south of
494 our study area (27°–35° S) and in a different segment of the SW Gondwana margin (*e.g.*,
495 Creixell *et al.*, 2025) with distinctive geodynamic events, including the accretion of the
496 Chilenia microplate (*e.g.*, Ramos *et al.*, 1986; Ramos, 2010; Boedo *et al.*, 2016).

497 Structural contact between the CLMC and the El Toco Formation

498 Given that the El Toco and Sierra del Tigre formations are low-grade metasedimentary rocks
499 (Bobenrieth, 1980; Breitkreuz and Bahlburg, 1985; Bahlburg *et al.*, 1987; Niemeyer *et al.*,
500 1997; Vásquez *et al.*, 2018), the contrasting higher metamorphic P-T conditions of the CLMC
501 imply that the contact between them is a major structural discontinuity, which uplifted the
502 western block (CLMC) relative to the eastern block (El Toco Formation). The timing of its
503 activity is constrained by the deposition of the Sierra de Lagunas Beds (Sepúlveda *et al.*,
504 2014), a Rhaetian-Pliensbachian volcano-sedimentary unit that unconformably covers both
505 the CLMC and the El Toco Formation, sealing the structure between them. Later, this major
506 structure was reactivated and incorporated as part of the main trace of the AFS during the
507 Early Cretaceous (*e.g.*, Scheuber and González, 1999; Grocott and Taylor, 2002).

508 Regional implications and tectonic event

509 The migmatisation event of the CLMC (*ca.* 318–316 Ma) forms part of a well-defined period
510 of magmatism in Late Mississippian-Early Pennsylvanian times at the SW Gondwana margin
511 (Maksaev *et al.*, 2014). Magmatism contemporaneous with migmatisation was recorded in
512 the Precordillera, at nearly the same latitude, by Aguilef *et al.* (2018) and Dahlström *et al.*
513 (2022), who obtained LA-ICP-MS U-Pb zircon ages of 316–310 Ma and *ca.* 315 Ma,
514 respectively. Dahlström *et al.* (2022) determined an emplacement pressure of ~3.2 kbar for
515 the same dated body (a hornblende-bearing granodiorite), similar to that obtained here for
516 the CLMC migmatites (~3.3–3.4 kbar). In contrast, the pressure of emplacement determined
517 by the same authors for many other younger intrusive bodies, from latest Carboniferous to
518 late Eocene in age, was only ~1.2–1.9 kbar. The congruence of age and pressure (depth) of
519 emplacement between migmatites and coeval intrusives, as opposed to emplacement
520 conditions for younger plutonic bodies, suggests that the former shared a
521 geodynamic/tectonic scenario where anatexis/magmatism occurred at deeper crustal
522 levels. Further studies are required to establish whether the coeval high-T event and
523 magmatism at 318–310 Ma (middle Carboniferous) in both the Coastal Cordillera and the
524 Precordillera originated in the same magmatic arc, or they represent independent coeval
525 events from different tectonic settings in the Gondwana margin. The first scenario would
526 imply that the CLMC was part of the 'migmatite front' (*sensu* Brown and Solar, 1999; Brown
527 *et al.*, 2011) of the middle Carboniferous magmatic arc. The emplacement depth is
528 consistent with crustal recycling during formation of upper Palaeozoic granites in northern
529 Chile (Lucassen *et al*., 1999), and the geothermal gradient of 52 °C/km deduced from the
530 metamorphic P-T conditions is coherent with upper crust (<10 km) geothermal gradients in

531 continental magmatic arcs (*e.g.*, Rothstein and Manning, 2003) and with gradients
532 associated with the formation of low-pressure/high-temperature metamorphic belts (De
533 Yoreo *et al.*, 1991; Takeshita and Okudaira, 1995).

534 The 'Toco Orogeny' (Bahlburg and Breitkreuz, 1991) affected all Upper Devonian-Lower
535 Carboniferous metasedimentary units in the Coastal Cordillera of northern Chile, which
536 were folded, deformed, and slightly metamorphosed (Bahlburg and Hervé, 1997). These
537 authors suggested that this deformation proceeded as the units were incorporated into the
538 Carboniferous accretionary prism of SW Gondwana. While the maximum age of this
539 deformative event is constrained by the youngest U-Pb detrital zircon age population in
540 these metasedimentary successions (*ca.* 350 Ma: El Toco Formation, Augustsson *et al*.,
541 2015; *ca*. 335 Ma: Sierra del Tigre Formation, Antofagasta Minerals *in* Baeza and Astudillo,
542 2019), the minimum age is restricted by undeformed Upper Carboniferous granites that
543 intrude the El Toco Formation. These plutonic bodies were dated using K-Ar in biotite at *ca.*
544 320–310 Ma (Maksaev and Marinovic, 1980; Skarmeta and Marinovic, 1981; Lucassen *et*
545 *al.*, 1999). However, more precise U-Pb zircon dating in recent years has yielded ages of *ca.*
546 302–301 Ma (Sepúlveda *et al.*, 2014; Vásquez *et al.*, 2018), indicating a pre-Late
547 Pennsylvanian (Gzhelian) age for the Toco tectonic event.

548 Considering the Early-Middle Mississippian maximum age for the 'Toco Orogeny', the
549 formation of migmatites of the CLMC at *ca.* 318–316 Ma (Early Pennsylvanian), and the
550 emplacement of undeformed plutonic bodies at *ca.* 302–301 Ma (Late Pennsylvanian), it is
551 highly probable that the compressional deformative event recorded in the CLMC was
552 essentially coeval with the 'Toco Orogeny'. Moreover, as shown here, the abundant

553 kinematic indicators of syn-anatectic strain in the CLMC (Fig. 2; Appendix B) show an
554 approximately westward (current coordinates) tectonic transport, which is nearly the same
555 vergence of folds and faults affecting the El Toco and Sierra del Tigre formations. The latter
556 units exhibit gently plunging overturned to recumbent chevron folds and minor concentric
557 folds, with axial planes with NW to NNW trends and 0° to 30° NE dips, and sub-horizontal
558 SW-vergent thrust faults (Maksaev and Marinovic, 1980; Boric, 1981; Skarmeta and
559 Marinovic, 1981; Niemeyer *et al.*, 1997), which, in sum, indicate an overall WSW- to SW-
560 vergence. These chronological and structural similarities, together with the fact that no
561 other Carboniferous tectonic events have so far been reported from this segment of the SW
562 Gondwana margin, allow us to infer that the tectonic event recorded during the generation
563 of the migmatites of the CLMC was, in fact, the 'Toco Orogeny'. This would constrain the
564 age of this tectonic event to the Early Pennsylvanian.

565 Taking into account the Early Mississippian (*ca.* 350 Ma) maximum depositional age of the
566 El Toco Formation, and the Early Pennsylvanian (*ca.* 318–316 Ma) migmatisation age of the
567 CLMC, forearc tectonic and sedimentary processes could have acted over up to ~30 Myr,
568 which saw incorporation of the sediments of the El Toco Formation into the upper crust and
569 development of migmatites at ~13 km. The forearc thermal anomaly responsible for the
570 generation of the CLMC is evidently associated with a compressional tectonic regime, as
571 shown by the kinematic indicators, a regime that contrasts with the extensional scenarios
572 proposed by Creixell *et al.* (2021). Niemeyer *et al.* (1997) also found evidence of extensional
573 tectonic deformation in rocks of the Sierra del Tigre Formation but showed that it developed
574 in soft sediments and was later overprinted by the SW-vergent compressive tectonic

deformation, which they attributed to its subsequent incorporation into the accretionary prism. A minimum thickness of ~2,300 m has been determined for the El Toco and Sierra del Tigre formations (Bahlburg and Breitkreuz, 1993; Niemeyer *et al.*, 1997). The depth of ~13 km for the migmatisation event necessarily implies a relatively fast increase in the crustal thickness of the forearc, which would require tectonics prevailing over sedimentary processes, with the former likely to be linked to thrusting of these units during the geodynamic evolution of the forearc. This is consistent with the inferred compressive tectonics during the migmatisation of the CLMC. The thermal input required to modify the geothermal gradient in the forearc and allow migmatisation in the upper crust must derive from the advection of heat of contemporaneous magmas (*e.g.*, Brown, 2013), most likely from the mantle or lower crust of SW Gondwana. There is currently no evidence to support other extra-continental sources of heat, such as subduction of a young oceanic plate or a spreading ridge.

Another case of Pennsylvanian migmatite formation at the SW Gondwana margin was recorded farther south (~33°S), at Las Cruces on the coast of central Chile, where Hervé *et al.* (2020) dated a garnet-bearing granitic neosome at *ca.* 320 Ma (U-Pb SHRIMP zircon age) and inferred a forearc tectonic setting for its sedimentary protolith. Despite the sparse evidence of such high-T metamorphic processes, it seems that migmatite formation in the forearc of the SW Gondwana margin was linked to major changes in subduction system dynamics, in connection with either the start of subduction in the Early Carboniferous (*ca.* 340–330 Ma; Creixell *et al.*, 2021) or the end of the Devonian magmatic lull (Bahlburg, 2022).

Conclusions

Migmatites of the CLMC formed at ~3.3–3.4 kbar and 650 °C. Kinematic indicators suggest compressional tectonic conditions during their generation in the Early Pennsylvanian (318–316 Ma). The inferred depth of the CLMC migmatisation event (~13 km) is coherent with that determined for coeval intrusive rocks cropping out in the Precordillera. It markedly contrasts with the shallower depths of post-Middle Pennsylvanian intrusive bodies emplaced in the upper crust of SW Gondwana.

U-Pb detrital zircon ages indicate that both the El Toco Formation and the protolith of the CLMC have maximum depositional ages in the Early Mississippian (*ca*. 350 Ma). The similarities in their overall U-Pb detrital zircon age pattern, and the proximity of their outcrops, suggest that the protolith of the CLMC is the El Toco Formation. These rocks were deposited at the margin of SW Gondwana and subsequently incorporated into the upper crust of the forearc by tectonic processes during the early–middle Carboniferous. Later anatexis of this unit occurred in the Early Pennsylvanian, associated with compressional tectonic conditions.

The structural similarities between the deformation registered in the CLMC and those present in the El Toco and Sierra del Tigre formations, together with their temporal constraints, allow us to infer that the 'Toco Orogeny' was the cause of the compressional tectonic conditions recorded during the generation of the migmatites of the CLMC in the Early Pennsylvanian.

The metamorphic P-T conditions determined for the CLMC imply that the structure that currently separates this unit from the El Toco Formation (the AFS) represents a major structural discontinuity. Prior to the Late Triassic, the CLMC was uplifted along this fault relative to the El Toco Formation outcrops, resulting in the juxtaposition of rocks with contrasting metamorphic conditions.

Acknowledgments

This study is part of the Chilean National Mapping Program (PNG) of the General Geology Department at Sernageomin. We are indebted to F. Lucassen for access to his samples of the CLMC. M. Calderón (Universidad del Desarrollo), H.-J. Massonne (Stuttgart Universität), and J. Álvarez (Sernageomin) are thanked for helping in thermodynamic calculations. C. Holmgren and E. Fonseca (Sernageomin) for assistance with opaque minerals petrography. A. Tomlinson (Sernageomin) for field support and fruitful discussions. F. LIona and A. Bustos (Sernageomin) performed the LA-ICP-MS analysis. M. Suárez (Sernageomin) conducted the EDS analyses. Thorough reviews by H. Bahlburg, C. Casquet, A. Willner, and editorial handling by R.J. Pankhurst and D. Bertin helped to greatly improve the original text.

References

Aguilef, S.; Franco, C.; Tomlinson, A.J.; Blanco, N.; Álvarez, J.; Montecino, D.; Gardeweg, M.; Campos, V.; Rodríguez, C.; Maksaev, V.; Bobadilla, H.; Vásquez, P.; Grunder, A.L.; Dilles, J.H. 2019. Geología del área Quehuita-Chela, regiones de Tarapacá y Antofagasta. SERNAGEOMIN, Carta Geológica de Chile, Serie Geología Básica 207: 293 p.

637 Augustsson, C.; Rüsing, T.; Niemeyer, H.; Kooijman, E.; Berndt, J.; Bahlburg, H.;
638 Zimmermann, U. 2015. 0.3 byr of drainage stability along the Palaeozoic palaeo-Pacific
639 Gondwana margin; a detrital zircon study. Journal of the Geological Society 172: 186-200.

640 Baeza, L.; Astudillo, N. 2019. Carta Pedro de Valdivia, Región de Antofagasta. Servicio
641 Nacional de Geología y Minería, Carta Geológica de Chile. Serie Geología Básica 206: 91 p.

642 Bahlburg, H. 2022. A Silurian-Devonian active margin in the proto-Andes - new data on an
643 old conundrum. International Geology Review 64 (21): 3099-3120.

644 Bahlburg, H.; Breitkreuz, C. 1991. The evolution of marginal basins in the southern Central
645 Andes of Argentina and Chile during the Paleozoic. Journal of South American Earth Sciences
646 4:171-188.

647 Bahlburg, H.; Breitkreuz, C. 1993. Differential response of a Devonian-Carboniferous
648 platform-deeper basin system to sea-level change and tectonics, N. Chilean Andes. Basin
649 Research 5: 21-40.

650 Bahlburg, H.; Hervé, F. 1997. Geodynamic evolution and tectonostratigraphic terranes of
651 northwestern Argentina and northern Chile. Geological Society of America Bulletin 109:
652 869-884.

653 Bahlburg, H.; Breitkreuz, C.; Zeil, W. 1987. Paleozoic basin development in northern Chile
654 (21°-27°S). Geologische Rundschau 76 (2): 633-646.

655 Bahlburg, H.; Vervoort, J.; Du Frane, S.; Bock, B.; Augustsson, C.; Reimann, C. 2009. Timing
656 of crust formation and recycling in accretionary orogens: Insights learned from the western
657 margin of South Amer*ica.* Earth-Science Reviews 97: 215-241.

658 Black, L.P.; Kamo, S.L.; Allen, C.M.; Davis, D.W.; Aleinikoff, J.N.; Valley, J.W.; Mundil, R.;
659 Campbell, I.H.; Korsch, R.J.; Williams, I.S.; Foudoulis, C. 2004. Improved 206Pb/218U
660 microprobe geochronology by the monitoring of a trace-element-related matrix effect;
661 SHRIMP, ID-TIMS, ELA-ICP-MS and oxygen isotope documentation for a series of zircon
662 standards. Chemical Geology 205: 115-140.

663 Bobenrieth, L. 1980. Geología de los cuadrángulos Cerro Desamparado y Cerro Soledad,
664 Regiones de Tarapacá y Antofagasta. Undergraduated Thesis, Universidad de Chile,
665 Departamento de Geología: 171 p. Santiago.

666 Boedo, F.; Willner, A.P.; Vurjovich, G.I.; Massonne, H-.J. 2016. High-pressure/low-
667 temperature metamorphism in the collision zone between the Chilenia and Cuyania
668 microcontinents (western Precordillera, Argentina). Journal of South American Earth
669 Sciences 72: 227-240.

670 Boric, R. 1981. Cuadrángulos Estación Colupito y El Toco, Región de Antolagasta. Instituto
671 de Investigaciones Geológicas, Carta Geológica de Chile, No. 49-50, 2 mapas 1 :50.000.
672 Santiago.

673 Breitkreuz, C.; Bahlburg, H. 1985. Paleozoic Flysch Series in the Coastal Cordillera of
674 Northern Chile. Geologische Rundschau 74 (3): 565-572.

675 Brown, M. 2013. Granite: From genesis to emplacement. GSA Bulletin 125 (7/8): 1079-1113.

676 Brown, M.; Solar, G.S. 1999. The mechanism of ascent and emplacement of granite magma
677 during transpression: a syntectonic granite paradigm. Tectonophysics 312: 1- 33.

678 Brown, M.; Korhonen, F.J.; Siddoway, C.S. 2011. Organizing melt flow through the crust.
679 Episodes 7 (4): 261-266.

680 Calderón, M; Hervé, F.; Munizaga, F.; Pankhurst, R.J.; Fanning, C.M.; Rapela, C.W. 2020.
681 Geochronological record of plutonic activity on a long-lived active continental margin, with
682 emphasis on the pre-Andean rocks of Chile. In Geocronologia e Evolução Tectônica do
683 Continente Sul-Americano: a contribuição de Umberto Giuseppe Cordani (Bartorelli, A.;
684 Teixeira, W.; de Brito Neves, B.B.; eds.). Solaris Edições Culturais, São Paulo. Capítulo18:
685 392-407.

686 Calle, A.Z., Horton, B.K.; García, R.; Anderson, R.B.; Stockli, D.F.; Flaig, P.P.; Long, S.P. 2023.
687 Sediment Dispersal and Basin Evolution During Contrasting Tectonic Regimes Along the
688 Western Gondwanan Margin in the Central Andes. Journal of South American Earth
689 Sciences 125: 104286. https://doi.org/10.1016/j.jsames. 2023.104286.

690 Cardona, A.; Cordani, U.G.; Ruiz, J.; Valencia, V.A.; Armstrong, R.; Chew, D.; Nutman, A.;
691 Sanchez, A.W. 2009. U-Pb zircon geochronology and Nd isotopic signatures of the pre-
692 Mesozoic metamorphic basement of the eastern Peruvian Andes: growth and provenance
693 of a late Neoproterozoic to carboniferous accretionary orogen on the northwest margin of
694 Gondwana. Journal of Geology 117: 285-305.

695 Cawood, P.A. 2005. Terra australis Orogen: Rodinia breakup and development of the Pacific
696 and Iapetus margins of Gondwana during the Neoproterozoic and Paleozoic. Earth Science
697 Reviews 69, 249-279.

698 Charrier, R.; Pinto, L.; Rodríguez, M.P. 2007. Tectonostratigraphic evolution of the Andean
699 Orogen in Chile. In The Geology of Chile (Moreno, T.; Gibbons, W.; eds.). The Geological
700 Society, London: 21-114.

701 Chen., D. 2010. Devonian-Carboniferous Carbonates around Guilin, South China:
702 Stratigraphy and Sedimentology. Guidebook for field excursion. *In* IGCP – 580 Meeting,
703 Applications of Magnetic Susceptibility on Paleozoic Rocks. Guilin, South China. 29 p.

704 Chen, D.; Qing, H. 2024. Devonian-Carboniferous Carbonates in Guilin, South China:
705 Depositional Records of Platform-Basin Complex and Major Biocrisises. In: Hu, X. (eds) Field
706 Trip Guidebook on Chinese Sedimentary Geology. Springer, Singapore. 809-871.

707 Chew, D.M.; Schaltegger, U.; Košler, J.; Whitehouse, M.J.; Gutjahr, M.; Spikings, R.A.;
708 Mišković, A. 2007. U-Pb geochronologic evidence for the evolution of the Gondwanan
709 margin of the north-central Andes. Geological Society of America Bulletin 119, 697-711.

710 Connolly, J.A.D., 2005. Computation of phase equilibria by linear programming: a tool for
711 geodynamic modeling and its application to subduction zone decarbonation. Earth and
712 Planetary Science Letters 236: 524-541.

713 Creixell, C.; Sepúlveda, F.; Álvarez, J.; Vásquez, P.; Velásquez, R. 2021. The Carboniferous
714 onset of subduction at SW Gondwana revisited: Sedimentation and deformation processes

along the late Paleozoic forearc of north Chile (21°–33° S). Journal of South American Earth Sciences 107: 103149.

Creixell, C.; Díaz-Alvarado, J.; Álvarez, J.; Rodríguez, C.; Velásquez, R.; Oliveros, V. 2025. Episodic magmatism and segmentation of the Gondwanan arc in Chile (21–38°S): Insights into Carboniferous to early Permian subduction processes and deformation. Journal of South American Earth Sciences 156: 105421.

Dahlquist, J.A.; Alasino, P.H.; Basei, M.; Morales Cámera, M.; Macchioli Grande, M.; da Costa Campos Neto, M. 2018. Petrological, geochemical, isotopic, and geochronological constraints for the Late Devonian-Early Carboniferous magmatism in SW Gondwana (27-32°LS): an example of geodynamic switching. International Journal of Earth Sciences 107: 2575-2603.

Dahlquist, J.A.; Morales Cámera, M.M.; Alasino, P.H.; Pankhurst, R.J.; Basei, M.A.S.; Rapela, C.W.; Moreno, J.A.; Baldo, E.G.; Galindo, C. 2021. A review of Devonian-Carboniferous magmatism in the central region of Argentina, Pre-Andean margin of SW Gondwana. Earth-Science Reviews 221: 103781. https:// doi. org/ 10. 1016/j. earsc irev. 2021. 103781.

Dahlström, S.I.R.; Cooper, F.J.; Blundy, J.; Tapster, S.; Yáñez, J.C.; Evenstar, L.A. 2022. Pluton exhumation in the Precordillera of northern Chile (17.8°–24.2°S): Implications for the formation, enrichment, and preservation of porphyry copper deposits. Economic Geology 117 (5): 1043-1071.

734 Dalziel, I.W.D.; Forsythe, R.D. 1985. Andean evolution and the terrane concept. In Howell,
735 D.G., ed., Tectonostratigraphic terranes of the Circum-Pacific-Region: Circum-Pacific-
736 Council for Energy and Mineral Resources, Earth Science Series 1: 565-581.

737 Damm, K.W.; Pichowiak, S.; Harmon, R.S.; Todt, W.; Kelley, S.; Omarini, R.; Niemeyer, H.
738 1990, Pre-Mesozoic evolution of the central Andes; The basement revisited. In Kay, S.M.,
739 and Rapela, C.W., eds., Plutonism from Antarctica to Alaska. Boulder, Colorado. Geological
740 Society of America: 101-125.

741 De Yoreo, J.J.; Lux, D.R.; Guidotti, C.V. 1991. Thermal modelling in low-pressure/high-
742 temperature metamorphic belts. Tectonophysics 188: 209-238.

743 Díaz-Alvarado, J.; Galaz, G.; Oliveros, V.; Creixell, C.; Calderón, M. 2019. Fragments of the
744 late Paleozoic accretionary complex in central and northern Chile: similarities and
745 differences as a key to decipher the complexity of the late Paleozoic to Triassic early Andean
746 events. In: Horton, B., Folguera, A. (Eds.), Andean Tectonics. Elsevier: 509–530.

747 Diener, J.F.A.; Powell, R. 2010. The influence of ferric iron on the stability of mineral
748 assemblages. Journal of Metamorphic Geology 28: 599-613.

749 Einhorn, J.C.; Gehrels, G.E.; Vernon, A.; DeCelles, P.G. 2015. U-Pb zircon geochronology of
750 Neoproterozoic-Paleozoic sandstones and Paleozoic plutonic rocks in the Central Andes
751 (21°S-26°S). *In* Geodynamics of a Cordilleran Orogenic System: The Central Andes of
752 Argentina and Northern Chile (DeCelles, P.G.; Ducea, M.N.; Carrapa, B.; Kapp, P.A.; editors).
753 Geological Society of America, Memoir 212: 115-124.

754 Ferraris, F.; Di Biase, F. 1978. Hoja Antofagasta, Región de Antofagasta. Instituto de
755 Investigaciones Geológicas, Carta Geológica de Chile, No. 30, 1 mapa 1:250.000.

756 Ferroni, F.; DeCelles, P.G.; Veramendi, J.O.; Dahlquist, J.A.; di Pasquo, M. 2025. New
757 Geochronological Constraints on the Late Palaeozoic Tarija Basin, Southern Bolivia: Tectonic
758 and Palaeoclimatic Implications. Terra Nova 38 (1): 9-18.

759 García Zavaleta, A., Hauser, N.; Roddaz, M.; Gonçalves, G.O.; Aparicio González, P.; Baby, P.;
760 Reimold, W.U.; Puma, F.; Bravo, P.; Humerez, M. 2024. Provenance of Devonian-
761 Carboniferous Sedimentary Rocks of the Tarija Basin, Southern Bolivia: Implications for the
762 Geodynamic Evolution of the Southwestern Margin of Gondwana. Geological Society of
763 America Bulletin 136 (3-4): 1730-1752.

764 Grocott, J.; Taylor, G.K. 2002. Deformation partitioning, magmatic arc fault systems and the
765 emplacement of granitic complexes in the Coastal Cordillera, north Chilean Andes (25-27°S).
766 Journal of Geological Society of London 159: 425-442.

767 Harrington, H.J. 1961. Geology of parts of Antofagasta and Atacama provinces of northern
768 Chile. American Association of Petroleum Geologist Bulletin 45 (2): 168-197.

769 Hawthorne, F.C.; Oberti, R.; Harlow, G.E.; Maresch, W.V.; Martin, R.F.; Schumacher, J.C.;
770 Welch, M.D. 2012. IMA report - nomenclature of the amphibole supergroup. American
771 Mineralogist 97: 2031-2048.

772 Hemmelmann, A. 2018. Petrologie und Mineralchemie des metamorphen andinen
773 Basements bei Caleta Loa, Nordchile. Bachelorarbeit, Technische Univeristät Berlin: 56 p.

774 Henry, D.J.; Guidotti, C.V.; Thomson, J.A. 2005. The Ti-saturation surface for low-to-medium
775 pressure metapelitic biotites: implications for geothermometry and Ti-substitution
776 mechanisms. American Mineralogist. 90 (2-3): 316-328.

777 Hervé, F.; Faundez, V.; Calderón, M.; Massonne, H.-J.; Willner, A.P.; Moreno, T. 2007.
778 Metamorphic and plutonic basement complexes. In: Gibbons, W. (Ed.), The Geology of
779 Chile. The Geological Society, London: 5-20.

780 Hervé, F.; Calderón, M.; Fanning, C.M.; Pankhurst, R.J.; Godoy, E. 2013. Provenance
781 variations in the Late Paleozoic accretionary complex of central Chile as indicated by detrital
782 zircons. Gondwana Research 23: 1122-1135.

783 Hervé, F.; Calderón, M.; Fanning, C.M.; Pankhurst, R.J.; Navarro, J. 2020. U-Pb SHRIMP
784 detrital zircon dating of metamorphic rocks in north–central Chile (28°-33°S): evidence for
785 Carboniferous and Triassic metamorphism in a subduction setting. Journal of South
786 American Earth Science 103: 102767.

787 Holland, T.J.B., Powell, R., 1991. A Compensated-Redlich-Kwong (CORK) equation for
788 volumes and fugacities of CO_2 and H_2O in the range 1 bar to 50 kbar and 100-1600◦C:
789 Contributions to Mineralogy and Petrology 109: 265-273.

790 Holland, T.J.B., Powell, R., 1998. An internally consistent thermodynamic data set for phases
791 of petrological interest. Journal of Metamorphic Geology 16: 309-343.

792 Holness, M.; Cesare, B.; Sawyer, E.W. 2011. Melted rocks under the microscope:
793 microstructures and their interpretation. Elements 7: 247-252.

794 Jackson, S.E.; Pearson, N.J.; Griffin, W.L.; Belousova, E.A. 2004. The application of laser
795 ablation-inductively coupled plasma-mass spectrometry to in situ U-Pb zircon
796 geochronology. Chemical Geology 211 (1): 47-69.

797 Loewy, S.; Connelly, J.; Dalziel, I. 2004. An orphaned basement block: The Arequipa-
798 Antofalla Basement of the central Andean margin of South Amer*ica.* Geological Society of
799 America, Bulletin 116 (1-2): 171-187.

800 Lucassen, F.; Laber, A.; Franz, G. 1994. Geology and petrology of metamorphic rocks from
801 the Preandean basement of northern Chile, 18°-24° S. In Congreso Geológico Chileno, No.
802 7, Actas I: 96-100.

803 Lucassen, F.; Wilke, H.-G.; Virarnonte, J.; Becchio, R.; Franz, G.; Laber, A.; Wernmer, K.;
804 Vroon, P. 1996. The paleozoic basement of the central andes (18°-26°S): a metamorphic
805 view. In International Symposium on Andean Geodynamics, No. 3, Abstract: 779-782. St.
806 Malo, France.

807 Lucassen, F., Franz, G., Thirlwall, M.F., Mezger, K. 1999. Crustal recycling of metamorphic
808 basement: late Palaeozoic granitoids of northern Chile (~22◦ S). Implications for the
809 composition of the Andean crust. Journal of Petrology 40 (10): 1527-1551.

810 Lucassen, F.; Becchio, R.; Wilke, H.G.; Franz, G.; Thirlwall, M.F.; Viramonte, J.; Wemmer, K.
811 2000. Proterozoic-Paleozoic development of the basement of the Central Andes (18-26°S) -
812 a mobile belt of the South American craton. Journal of South American Earth Sciences 13:
813 697-715.

814 Lucassen, F.; Becchio, R.; Harmon, R.; Kasemann, S.; Franz, G.; Trumbull, R.; Wilke, H.G.;
815 Romer, R.L.; Dulski, P. 2001. Composition and density model of the continental crust at an
816 active continental margin: The Central Andes between 21° and 27°S. Tectonophysics 341:
817 195-223.

818 Ludwig, K.R. 2012. User's manual for Isoplot, Version 3.75, A geochronological toolkit for
819 Microsoft Excel. Berkeley Geochronology Center, Special Publication 5: 75 p. California.

820 Maksaev, V., Marinovic, N. 1980. Cuadrángulos Cerro de la Mica, Quillagua, Cerro Posada y
821 Oficina Prosperidad, Región de Antofagasta. Instituto de Investigaciones Geológicas. Carta
822 Geológica de Chile 45-48: 63 p., 4 mapas escala 1:50.000. Santiago.

823 Maksaev, V.; Munizaga, F.; Tassinari, C. 2014. Timing of the magmatism of the paleo-Pacific
824 border of Gondwana: U-Pb geochronology of Late Paleozoic to Early Mesozoic igneous rocks
825 of the north Chilean Andes between 20° and 31° S. Andean Geology 41 (3): 447-506

826 Massonne, H.-J. 2013. Constructing the pressure–temperature path of ultrahigh-pressure
827 rocks. Elements 9: 267-279.

828 Massonne H.-J.; Willner, A.P.; Gerya, T. 2007. Densities of metapelitic rocks at high to
829 ultrahigh pressure conditions: what are the geodynamic consequences? Earth and
830 Planetary Science Letters 256: 12-27.

831 Moisan, P.; Niemeyer, H.; Kerp, H. 2011. Lycopsids from the Upper Devonian of northern
832 Chile with remarks on the geographical distribution of the morphogenus *Haplostigma*
833 Seward. Paläontologische Zeitschrift 85: 231-240.

834 Mpodozis, C.; Ramos, V.A. 1989. The Andes of Chile and Argentina. In Ericksen, G.E., Cañas
835 Pinochet, M.T., Reinemund, J.A., eds. Geology of the Andes and its relation to hydrocarbon
836 and mineral resources. Circum Pacific Council for Energy and Mineral Resources, Earth
837 Science Series 11: 59-90.

838 Niemeyer, H.; Venegas, R.; González, C.; Aceñolaza, F. 1997. Los terrenos paleozoicos del
839 Salar de Navidad, Región de Antofagasta, Chile. Revista Geológica de Chile 24 (2): 123-143.

840 Pankhurst, R.J.; Rapela, C.W.; Saavedra, J.; Baldo, E.; Dahlquist, J.; Pascua, I.; Fanning, C.M.
841 1998. The Famatinian magmatic arc in the southern Sierras Pampeanas. *In* Pankhurst, R.J.;
842 Rapela, C.W. (eds), The Proto-Andean Margin of Gondwana. Special Publication of the
843 Geological Society, London 142: 343-367.

844 Pankhurst, R.; Hervé, F.; Fanning, C.M.; Calderón, M.; Niemeyer, H.; Griem-Klee, S.; Soto, F.
845 2016. The pre-Mesozoic rocks of northern Chile: U–Pb ages, and Hf and O isotopes. Earth-
846 Science Reviews 152: 88-105.

847 Pawley, M.; Reid, A.; Dutch, R.; Preiss, W. 2015. Demystifying migmatites: introduction for
848 field-based geologist. Applied Earth Science 124 (3): 147-174.

849 Petrus, J.A.; Kamber, B.S. 2012. VizualAge: A novel approach to laser ablation ICP-MS U-Pb
850 geochronology data reduction. Geostandards and Geoanalytical Research 36 (3): 247-270.

851 Powell, R.; Holland, T. 1999. Relating formulations of the thermodynamics of mineral solid
852 solutions: activity modeling of pyroxenes, amphiboles and micas. American Mineralogist 84:
853 1-14.

Ramos, V.A. 2008. The Basement of the Central Andes: The Arequipa and Related Terranes. Annual Review of Earth and Planetary Sciences 36: 289-324

Ramos, V.A., 2009. Anatomy and global context of the Andes: Main geologic features and the Andean orogenic cycle. *In* Kay, S.M., Ramos, V.A., and Dickinson, W.R., eds., Backbone of the Americas: Shallow Subduction, Plateau Uplift, and Ridge and Terrane Collision: Geological Society of America Memoir 204: 31-65.

Ramos, V.A. 2010. The Grenville-age basement of the Andes. Journal of South American Earth Sciences 29: 77-91.

Ramos, V.A.; Jordan, T.E.; Allmendinger, R.W.; Mpodozis, C.; Kay, S.; Cortés, J.M.; Palma, M. 1986. Paleozoic terranes of the central Argentine-Chilean Andes. Tectonics 5: 855-880.

Rapela, C.W.; Pankhurst, R.J.; Casquet, C.; Dahlquist, J.A.; Fanning, C.M.; Baldo, E.G.; Galindo, C.; Alasino, P.H.; Ramacciotti, C.D.; Verdecchia, S.O.; Murra, J.A.; Basei, M.A.S. 2018. A review of the Famatinian Ordovician magmatism in southern South America: evidence of lithosphere reworking and continental subduction in the early proto-Andean margin of Gondwana. Earth-Science Reviews 187: 259-285

Reimann, C.R.; Bahlburg, H.; Kooijman, E.; Berndt, J.; Gerdes, A.; Carlotto, V.; López, S. 2010. Geodynamic evolution of the early Paleozoic Western Gondwana margin 14–17°S reflected by the detritus of the Devonian and Ordovician basins of southern Peru and northern Bolivia. Gondwana Research 18: 370-384.

873 Rothstein, D.A.; Manning, C.E. 2003. Geothermal gradients in continental magmatic arcs:
874 constraints from the eastern Peninsular Ranges Batholith, Baja California, Mexico.
875 Geological Society of America Special Paper 374: 337-354.

876 Sawyer, E.W. 2008. Atlas of Migmatites. Canadian Mineralogist Special Publication 9, NRC
877 Research Press, Ottawa, Ontario, Canada.

878 Scheuber, E.; González, G. 1999. Tectonics of the Jurassic Early Cretaceous magmatic arc of
879 the north Chilean Coastal Cordillera (22° -26°S): A story of crustal deformation along a
880 convergent plate boundary. Tectonics 18 (5): 895-910.

881 Sepúlveda, F.A.; Vásquez, P.; Quezada, A. 2014. Cartas Patillos y Oficina Victoria, Región de
882 Tarapacá. SERNAGEOMIN, Carta Geológica de Chile, Serie Geología Básica 167-168: 125 p.,
883 1 mapa escala 1:100.000. Santiago.

884 Sepúlveda, F.; González, E.; Tomlinson, A.J. 2024. Geología y estructura del cuadrángulo
885 Quebrada Arcas, región de Antofagasta, Chile. Servicio Nacional de Geología y Minería,
886 Informe Registrado IR-23-108: 53 p., 1 mapa escala 1:50.000. Santiago.

887 Sernageomin. 2002. Mapa Geológico de Chile. 1:1.000.000. Carta Geológica de Chile, Serie
888 Geología Básica n° 75. Santiago.

889 Skarmeta, J.; Marinovic, N. 1981. Geología de la Hoja Quillagua, Región de Antofagasta.
890 Instituto de Investigaciones Geológicas, Carta Geológica de Chile 51: 63 p., 1 mapa escala
891 1:250.000. Santiago.

892 Stevens, G.; Villaros, A.; Moyen, J.-F. 2007. Selective peritectic garnet entrainment as the
893 origin of geochemical diversity in S-type granites. Geology 35 (1): 9-12.

894 Suárez, M.; Ramírez, C.; Cortés, R.; Llona, F.; Creixell, C.; Ramírez, A.; Vásquez, C. 2015.
895 Desarrollo de una nueva técnica de separación de circones mediante la incorporación de
896 fluorescencia en estudios de datación U-Pb. *In* XIV Congreso Geológico Chileno, Actas I: 703-
897 706.

898 Takeshita, T.; Okudaira, T. 1995. Dynamics and thermal modeling in low-pressure/high-
899 temperature metamorphic belts. Journal of the Seismological Society of Japan, Second
900 Series 47 (4): 453-467.

901 Torsvik, T.H., Cocks, L.R.M. 2013. Gondwana from top to base in space and time. Gondwana
902 Research 24: 999-1030.

903 Vásquez, P.; Sepúlveda, F.; Quezada, A.; Franco, C.; Blanco, N. 2018. Cartas Guanillos del
904 Norte y Salar de Llamara, Regiones de Tarapacá y Antofagasta. SERNAGEOMIN, Carta
905 Geológica de Chile, Serie Geología Básica 195-196: 93 p. 1 mapa escala 1:100.000. Santiago.

906 Vaughan, A.P.M.; Leat P.T.; Pankhurst, R.J. 2005. Terrane processes at the margins of
907 Gondwana: an introduction. Geological Society Special Publication 246: 1-22. London.

908 Vermeesch, P., 2018. IsoplotR: a free and open toolbox for geochronology. Geoscience
909 Frontiers 9: 1479-1493.

910 Vermeesch, P. 2021. Maximum depositional age estimation revisited. Geoscience Frontiers
911 12: 843-850.

912 White, R.W., Powell, R., and Holland, T.J.B. 2001. Calculation of partial melting equilibria in
913 the system Na2O-CaOK2O-FeO-MgO-Al2O3-SiO2-H2O (NCKFMASH). Journal of
914 Metamorphic Geology 19: 139-153.

915 White, R.W.; Pomroy, N.E.; Powell, R. 2005. An in situ metatexite–diatexite transition in
916 upper amphibolite facies rocks from Broken Hill, Australia. Journal of Metamorphic Geology
917 23: 579-602.

918 Wilke, H.; Lucassen, F.; Wemmer, H. 1997. Chemistry and isotopic ages of metamorphic
919 basement and intrusions. In Congreso Geológico Chileno, No. 8, Actas 2: 1593-1597.
920 Antofagasta.

921 Williams, I.S. 1998. U-Th-Pb geochronology by ion microprobe. *In* Applications of
922 Microanalytical Techniques to Understanding Mineralizing Processes (McKibben, M.A.;
923 Shanks III, W.C.; Ridley, W.I.; editors). Reviews in Economic Geology 7: 1-35.

924 Wu, C.M.; Chen, H.X. 2015. Revised Ti-in-biotite geothermometer for ilmenite- or rutile-
925 bearing crustal metapelites. Science Bulletin 60 (1): 116-121.

926

927 **Figure captions**

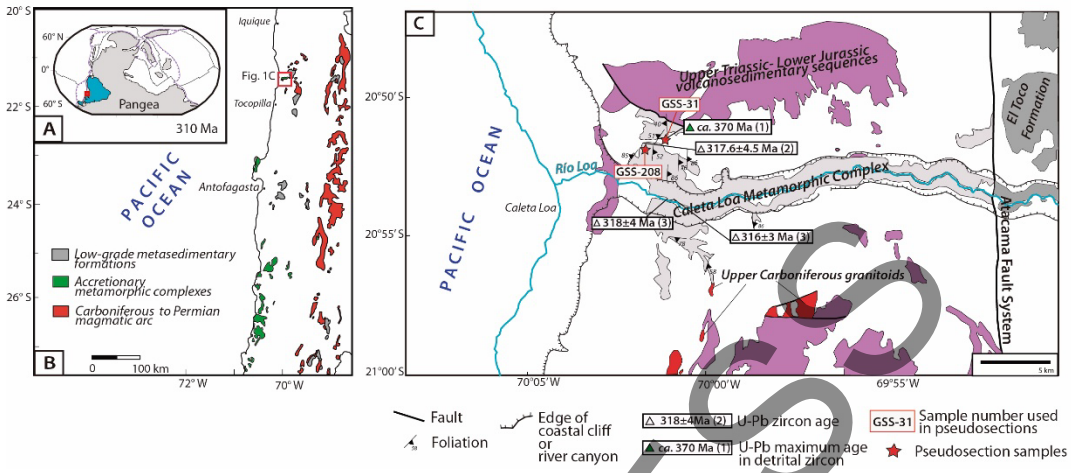

928

929 **Fig. 1. A.** Palaeographic reconstruction of Pangea at 310 Ma (Torsvik and Cocks, 2013). The
930 red square shows the approximate location of panel B, and the cyan area refers to the South
931 American continent. **B.** Location and regional geological context of upper Palaeozoic units
932 (modified from Creixell *et al*., 2021). The red square indicates the location of the study
933 region. **C.** Schematic geological map of the CLMC area (after Vásquez *et al.*, 2018). U-Pb
934 zircon ages from: (1) this study, (2) Vásquez *et al*. (2018), and (3) Pankhurst *et al*. (2016).

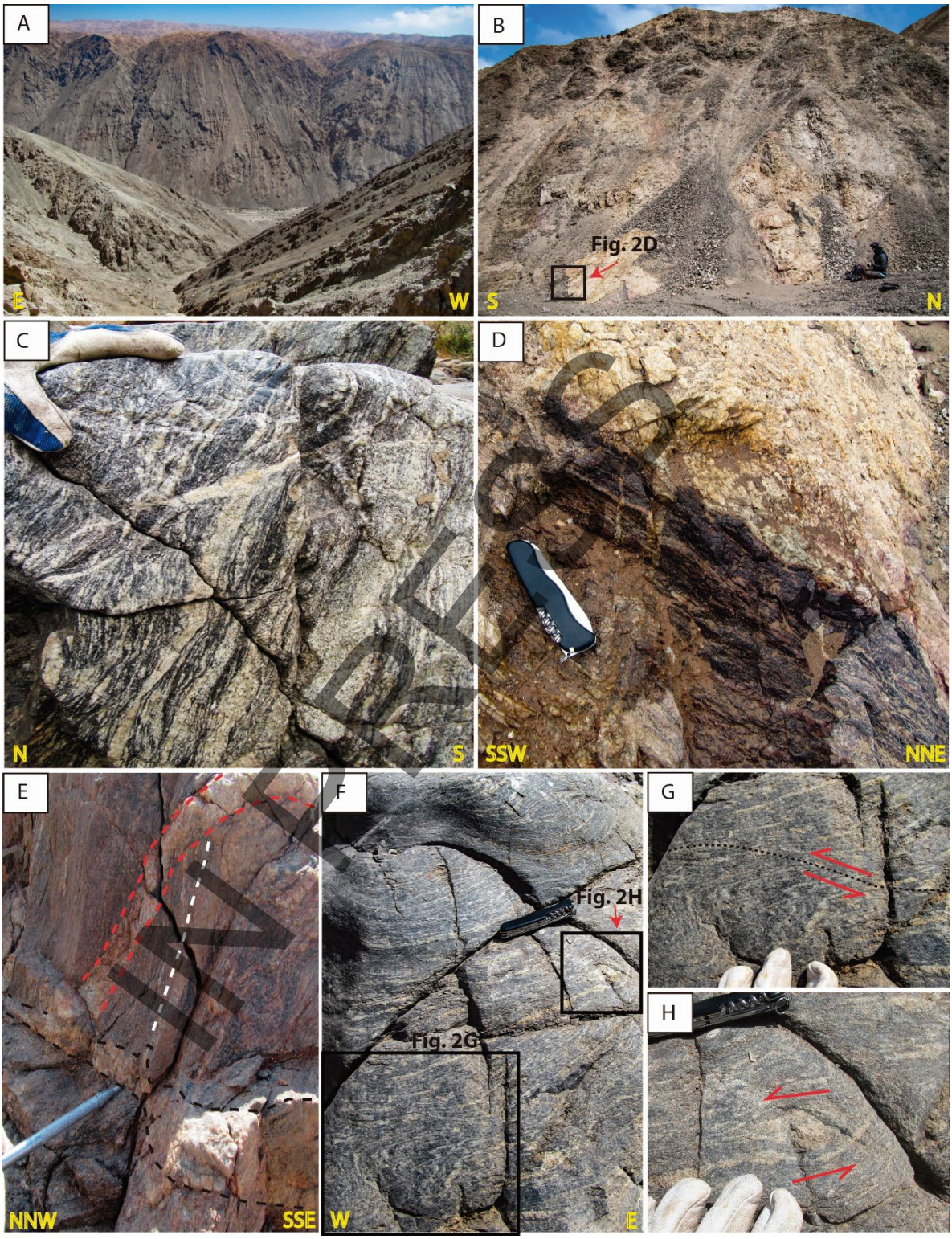

935

936 **Fig. 2.** Outcrop photographs of the CLMC. **A.** General view with the Río Loa at the bottom

937 of the canyon. **B.** Metric-scale leucosome (whitish yellow to pale pink) emplaced in

938 melanosome (dark grey). **C.** Average banded migmatite, with parallel coarse-grained
939 leucocratic bands, as well as coeval melt-filled shear zone cutting the banding at low angle.
940 **D.** Detailed view of B, showing subvertical veinlets of leucosome feeding the leucosome
941 blob. **E.** Textural continuity between cross-cutting band (black dashed lines) and low-angle
942 veins of leucosome (red dashed lines), with white dashed line showing the main foliation.
943 **F.** Stromatic migmatite with top-to-the west shear indicators, including albite porphyroblast
944 with sigma structure (right, centre) and folds associated with a low-angle shear zone (left,
945 bottom). **G.** Detail of F showing shear zone and folds indicating top-to-the west thrusting
946 (dashed black line). Note that folds are affected by S_2 foliation. **H.** Centimetric albite
947 porphyroblast with sigma structure indicating top-to-the west sense of shear.

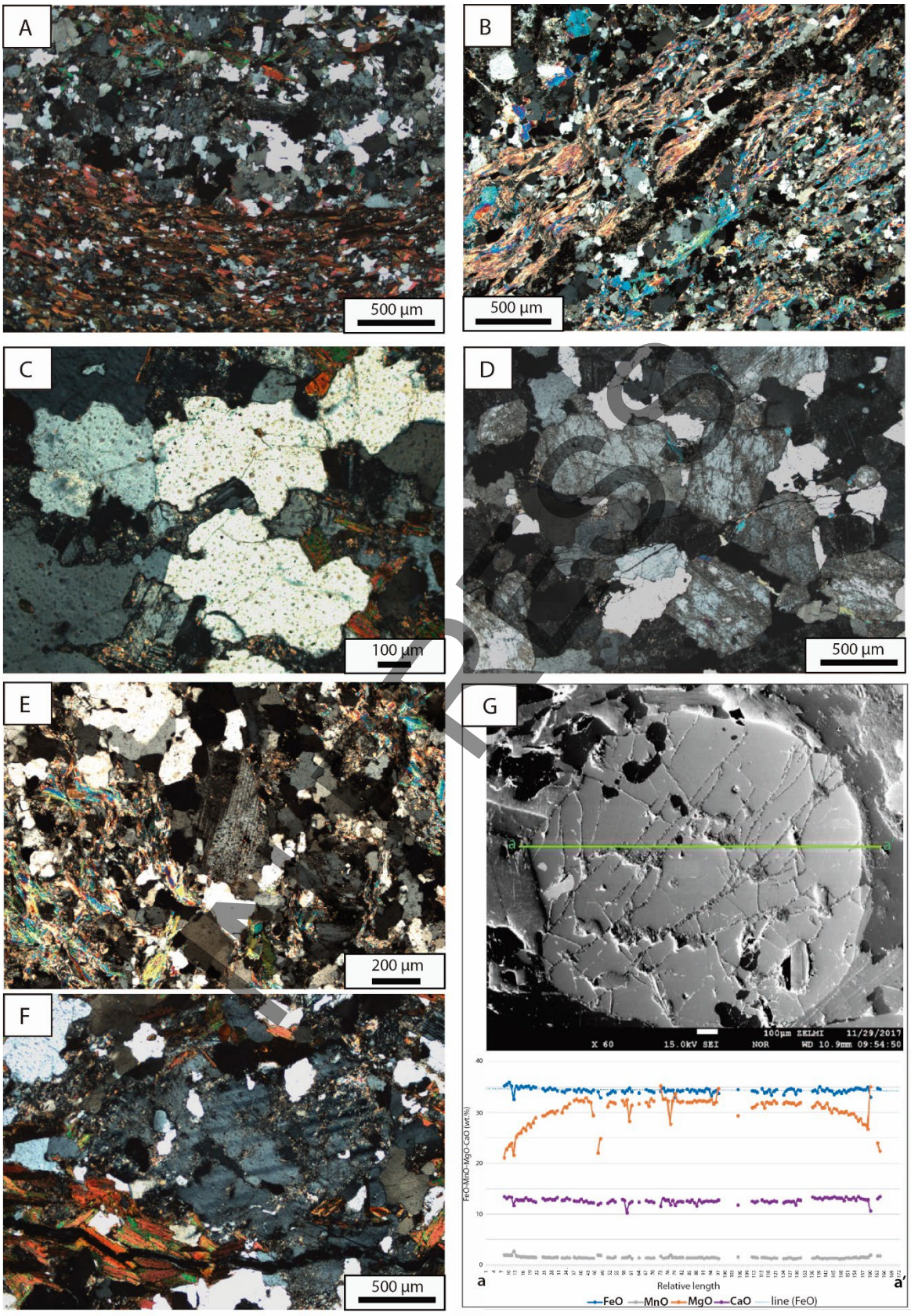
A
500 μm
B
500 μm
C
100 μm
D
500 μm
E
200 μm
F
500 μm
G
a
a'
X 60
15.0kV SEI
NOR
100μm ZELMI
11/29/2017
WD 10.9mm 09:54:50
FeO-MnO-MgO-CaO (wt.%)
40
30
20
10
0
a
a'
Relative length
FeO
MnO
MgO
CaO
line (FeO)

948

949 **Fig. 3.** Representative thin sections (**A-F**) and BSE image (**G**) of the CLMC. **A.** General view
950 of lepidogranoblastic domains with biotite defining the foliation and typical lobated
951 textures of mineral grains (sample GSS-185, crossed polars). **B.** Anastomosing foliation with
952 muscovite replacing sillimanite (fibrolite) crystals (sample PPV-14, crossed polars). **C.** Details
953 of "branching" plagioclase in quartz, together with lobate textures (sample GSS-185,
954 crossed polars). **D.** Typical granitic leucosome, with interstitial muscovite, branching K-
955 feldspar (top to the right), and cuspate quartz with low dihedral angle (right in centre)
956 (sample GSS-197, crossed polars). **E.** Deformation twins in plagioclase and string of beads
957 (centre-right) (sample PPV-14, crossed polars). **F.** Corroded plagioclase crystal (sample GSS-
958 185, crossed polars). **G.** BSE image of garnet (sample 3/278), showing element distribution
959 (in wt.%) along the profile *a*-*a'*.

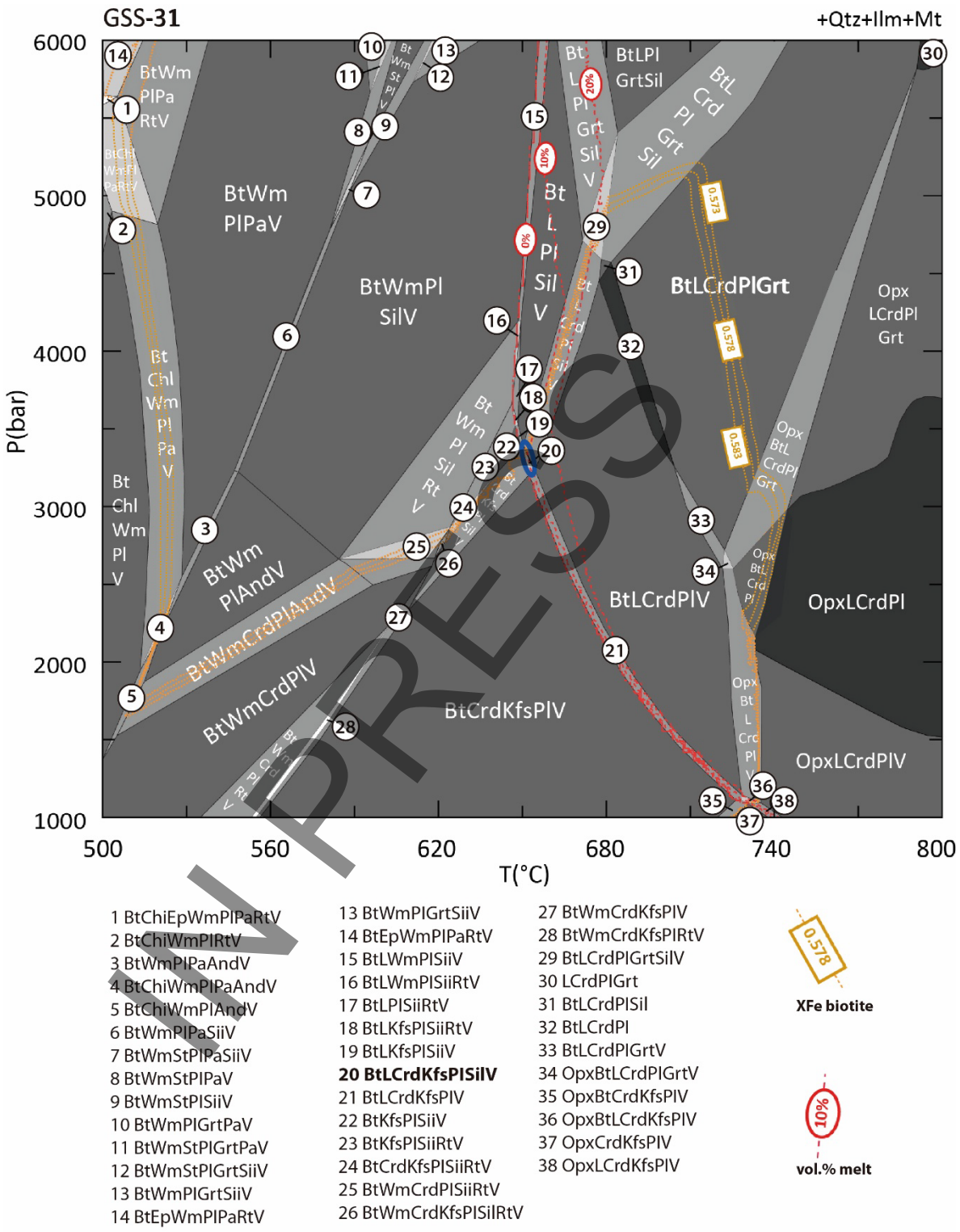

1 BtChiEpWmPlPaRtV
2 BtChiWmPlRtV
3 BtWmPlPaAndV
4 BtChiWmPlPaAndV
5 BtChiWmPlAndV
6 BtWmPlPaSiiV
7 BtWmStPlPaSiiV
8 BtWmStPlPaV
9 BtWmStPlSiiV
10 BtWmPlGrtPaV
11 BtWmStPlGrtPaV
12 BtWmStPlGrtSiiV
13 BtWmPlGrtSiiV
14 BtEpWmPlPaRtV
15 BtLWmPlSiiV
16 BtLWmPlSiiRtV
17 BtLPlSiiRtV
18 BtLKfsPlSiiRtV
19 BtLKfsPlSiiV
20 BtLCrdKfsPlSilV
21 BtLCrdKfsPlV
22 BtKfsPlSiiV
23 BtKfsPlSiiRtV
24 BtCrdKfsPlSiiRtV
25 BtWmCrdPlSiiRtV
26 BtWmCrdKfsPlSilRtV
27 BtWmCrdKfsPlV
28 BtWmCrdKfsPlRtV
29 BtLCrdPlGrtSilV
30 LCrdPlGrt
31 BtLCrdPlSil
32 BtLCrdPl
33 BtLCrdPlGrtV
34 OpxBtLCrdPlGrtV
35 OpxBtCrdKfsPlV
36 OpxBtLCrdKfsPlV
37 OpxCrdKfsPlV
38 OpxLCrdKfsPlV

960

961 **Fig. 4.** Pseudosection of sample GSS-31. Peak metamorphic assemblage in bold letters. Blue

962 ellipse marks the peak P-T conditions. Red segmented lines represent the calculated vol.%

963 of melt. Orange dotted lines represent the XFe of biotite. Shading indicates degree of
964 variance: white, divariant; light grey, trivariant; medium grey, quadrivariant; dark grey:
965 quintvariant. And: andalusite, Bt: biotite, Chl: chlorite, Crd: cordierite, Ep: epidote, Grt:
966 garnet, Ilm: ilmenite, Kfs: K-feldspar; L: melt, Mt: magnetite, Opx: orthopyroxene, Pa:
967 paragonite, Pl: plagioclase, Qtz: quartz, Sill: sillimanite, St: staurolite, Ru: rutile, V: H_2O, and
968 Wm: muscovite.

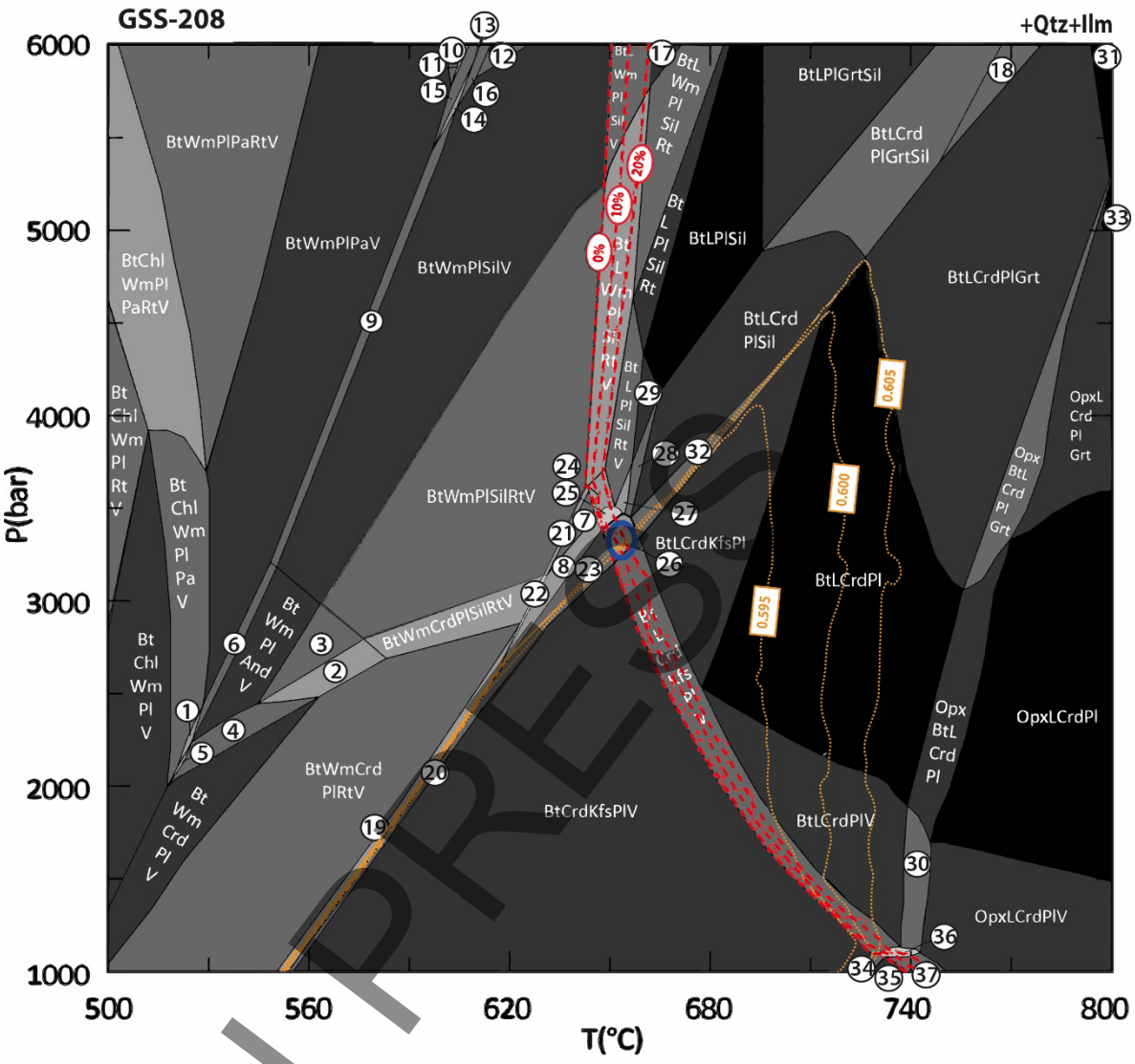

1 BtChlWmPlPaAndV
2 BtWmCrdPlAndRtV
3 BtWmPlAndRtV
4 BtWmCrdPlAndV
5 BtWmCrdPlPaAndV
6 BtWmPlPaAndV
7 BtKfsPlSilRtV
8 BtCrdKfsPlSilRtV
9 BtWmPlPaSilV
10 BtWmPlGrtPaV
11 BtWmStPlGrtPaV
12 BtWmPlGrtSilV
13 BtWmStPlV
14 BtWmStPlPaSilV
15 BtWmStPlPaV
16 BtWmStPlSilV
17 BtLWmPlSil
18 BtLCrdKfsPlGrt
19 BtWmCrdKfsPlRtV
20 BtWmCrdKfsPlV
21 BtWmKfsPlSilRtV
22 BtWmCrdKfsPlSilRtV
23 BtCrdKfsPlSilV
24 BtLKfsPlSilRtV
25 BtLCrdKfsPlSilRtV
26 BtLCrdKfsPlSilV
27 BtLCrdPlSilRtV
28 BtLCrdPlSilV
29 BtLPlSilV
30 OpxBtLCrdPlV
31 BtLCrdGrt
32 BtLCrdKfsPlSil
33 OpxLCrdGrt
34 OpxBtCrdKfsPlV
35 OpxCrdKfsPlV
36 OpxBtLCrdKfsPlV
37 OpxLCrdKfsPlV

0.578 XFe biotite

10% vol.% melt

969

970 **Fig. 5.** Pseudosection of sample GSS-208. Peak metamorphic assemblage in bold letters.
971 Blue ellipse marks the peak P-T conditions. Red segmented lines represent the calculated
972 vol.% of melt. Orange lines represent the XFe of biotite. Shading and mineral abbreviations
973 as in figure 4. Black shading: sextivariant.

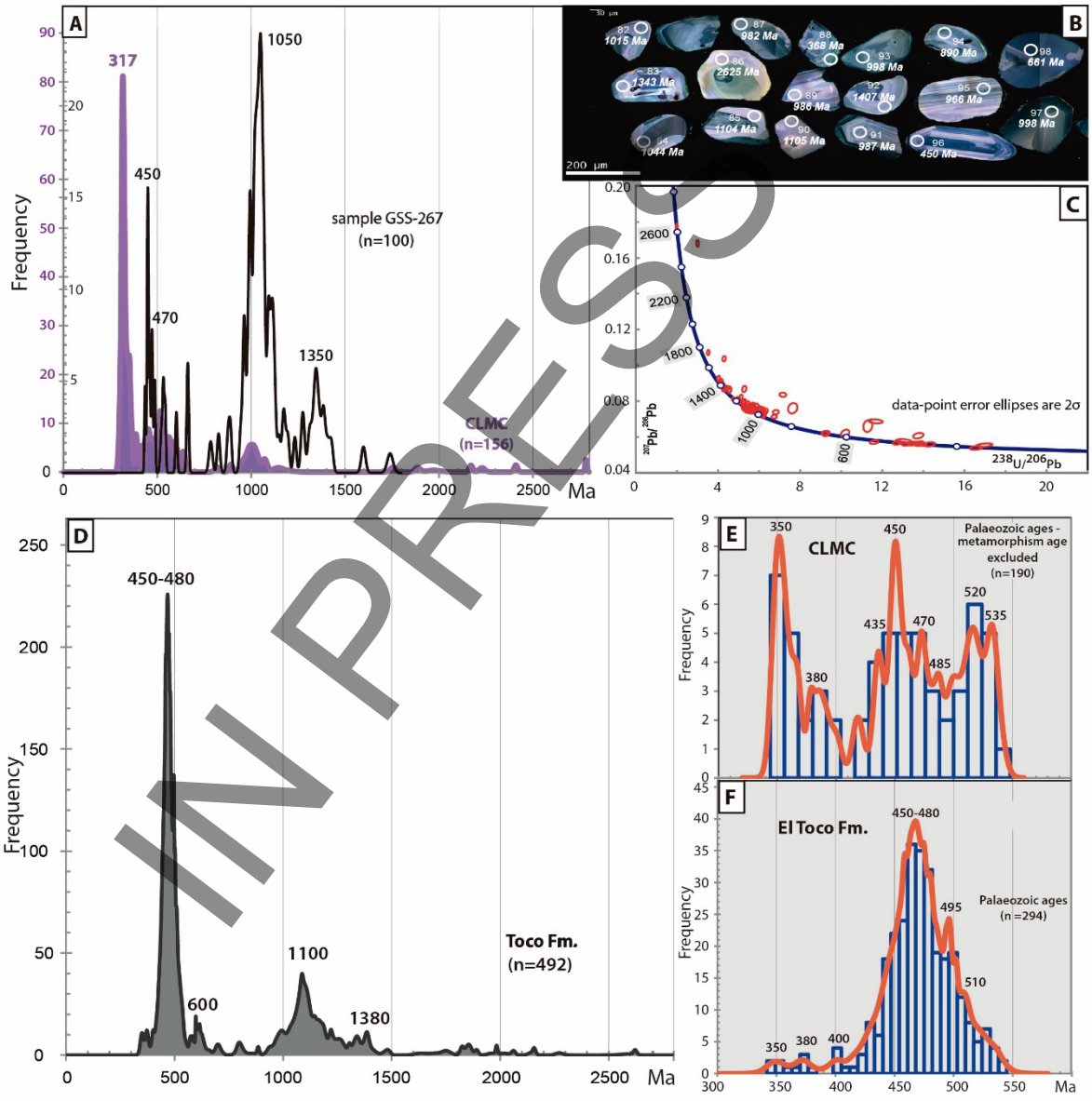

974

975 **Fig. 6. A.** Probability density plots with age histogram showing U-Pb zircon age distribution
976 of sample GSS-267 (black line) and composite U-Pb zircon age distribution of the CLMC
977 (purple), including data from Pankhurst *et al.* (2016) and Vásquez *et al.* (2018). **B.** Illustrative

CL images of dated zircon grains (U-Pb ages in italics, below the zircon grain number) from sample GSS-267. **C.** Tera-Wasserburg plots of uncorrected U-Pb data for sample GSS-267. **D.** Composite U-Pb zircon age distribution of the El Toco Formation, based on literature data (Bahlburg *et al.,* 2009; Augustsson *et al.,* 2015; Einhorn *et al.,* 2015). **E.** Composite U-Pb zircon age distribution of Palaeozoic ages (<539 Ma) from the CLMC, excluding ages for metamorphism of this complex. **F.** Composite U-Pb zircon age distribution of Palaeozoic ages (<539 Ma) from the El Toco Formation. Age scale in E as in F.

Table 1. CLMC samples, locations, mineral assemblages, and methods applied in this study.

Sample	UTM coordinates		Geographic coordinates		Metamorphic phases										Accesory phases		Pseudosections	Geothermometer	U-Pb dating
	E	N	W	S	Quartz	Plagioclase	K-felspar	Biotite	Sillimanite	Garnet	Cordierite	Ilmenite	Amphibole	Muscovite[1]	Chlorite[1]	F-Apatite	Monzonite		Ti in Biotite	
GSS-31	394691	7631771	70°0'57"	21°24'47"	x	x	x	x	x			x		x			x	x	x	
GSS-208	394209	7631272	70°1'14"	21°25'3"	x	x	x	x	x		x	x		x		x	x	x	x	
GSS-267	395066	7632192	70°0'44"	21°24'34"	x	x	x	x				x		x						x
3/276(*)	397780	7629614	69°59'11"	21°25'58"	x	x		x					x	x	x				x	
3/278(*)	397772	7629516	69°59'11"	21°26'2"	x	x		x		x		x		x		x				
3/347(*)	397587	7629534	69°59'17"	21°26'1"	x	x		x		x				x	x				x	

(*)approximate location

[1]retrograde phase

Table 2. Whole-rock and mineral chemistry of migmatite samples from the CLMC.

Sample	Whole-rock composition		Representative mineral analyses*										
			GSS-31							GSS-208			
Mineral phase (analysis n°)	GSS-31	GSS-208	Biotite (5)	Biotite (6)	White mica (4)	White mica (14)	Plagioclase (10)	Plagioclase (12)	Sillimanite (1)	Biotite (1)	White mica (5)[1]	White mica (6)[1]	Ilmenite (3)
SiO_2	71,22	73,90	34,39	34,57	44,25	45,02	62,57	60,17	36,83	34,96	46,37	46,81	0,00
Al_2O_3	12,58	12,11	19,77	8,13	35,38	36,25	23,01	24,98	62,46	19,24	35,86	36,18	0,24
TiO_2	0,97	0,82	2,59	2,94	0,21	1,19	0,02	0,01	0,01	1,85	0,30	0,01	56,67
FeO			20,06	20,39	1,03	0,74	0,07	0,07	0,17	21,03	0,80	1,69	34,59
Fe_2O_3	5,13	4,84											
CaO	1,34	0,62	0,04	0,02	0,05	0,00	3,64	5,70	0,03	0,00	0,00	0,00	0,09
MgO	1,59	1,91	8,42	8,13	0,66	0,42	0,00		0,02	7,77	0,00	0,00	0,10
MnO	0,04	0,04	0,15	0,16	0,03	0,00	0,01		0,00	0,16	0,43	0,99	2,43
Na_2O	2,24	1,28	0,22	0,23	0,44	0,47	9,76	8,58	0,00	0,00	0,00	0,00	0,00
K_2O	2,08	2,98	9,02	9,19	10,50	10,02	0,09	0,14	0,20	9,24	9,91	8,42	0,27
P_2O_5	0,12	0,12											
Total	97,30	98,62	94,66	95,29	92,55	94,11	99,15	99,66	99,71	94,66	93,67	94,10	94,77
Cations													
Si			5,287	5,291	3,034	3,020	2,791	2,688	0,998	5,419	3,106	3,105	0,039
Na			0,060	0,068	0,059	0,062	0,844	0,743	0,000	0,000	0,000	0,000	0,000
Ca			0,070	0,003	0,004	0,000	0,174	0,273	0,001	0,000	0,000	0,000	0,035
K			1,769	1,794	0,918	0,857	0,005	0,008	0,007	1,827	0,847	0,712	2,946
Fe			2,579	2,610	0,059	0,042	0,003	0,003	0,004	2,726	0,045	0,095	0,210
Mn			0,020	0,021	0,002	0,000	0,000	0,000	0,000	0,021	0,000	0,000	0,015
Mg			1,929	1,854	0,068	0,042	0,000	0,000	0,001	1,795	0,042	0,097	0,029
Al			3,583	3,547	2,860	2,866	1,210	1,315	1,996	3,516	2,831	2,828	4,340
Ti			0,299	0,338	0,011	0,060	0,001	0,000	0,000	0,215	0,015	0,001	7,624
Al^{IV}			2,713	2,709	0,966	0,981					0,894	0,895	
Al^{VI}			0,870	0,839	1,894	1,885					1,937	1,932	
F													0,010
Sum			15,544	15,526	7,015	6,947	5,028	5,030	3,007	15,512	6,886	6,838	15,248
Albite							83	73					
Orthoclase							1	1					
Anorthite							16	26					
Fe/(Fe+Mg)			0,572	0,585						0,603			
Mg+Fe					0,127	0,084					0,087	0,192	

All concentrations in wt.%

*Cations calculated on the basis of: 22 oxygens (biotite), 11 oxygens (white mica), and 8 oxygen (plagioclase) in structural formulae

[1]muscovite analysis shows a deficit in the interlayer cations

[2]muscovite analysis shows that the sum of divalent cations (Mg+Fe) is too low for its Si content

988 **Table 2.** Whole-rock and mineral chemistry of migmatite samples from the CLMC.

989

Appendix

A. Whole rock and mineral chemistry methodologies.

B. Photographs of CLMC outcrops and shear indicators.

Supplementary material

Supplementary Table 1. EDS analyses of samples GSS-31 and GSS-208.

Supplementary Table 2. Mineral chemistry determined by WDS EMPA.

Supplementary Table 3. U-Pb zircon age data of sample GSS-267.

Supplementary Table 4. U-Pb zircon age data and Maximum Likelihood Ages (MLA) of selected samples from Augustsson *et al*. (2015).